Chapter 2
Beam Optics and Orbits: Methods Used at the Tevatron Accelerators

V. Lebedev, V. Shiltsev, and A. Valishev

The success of the Tevatron Run II would not be possible without detailed work on the linear and nonlinear beam optics. The scope of optics work included all major stages: the optics design, optics measurements, and optics correction. Optics of all transport lines and rings was measured and corrected. This work resulted in a significant reduction of the emittance growth for beam transfers and increased the acceptances of the rings and transfer lines. The most spectacular improvements are related to the improvements of antiproton beam transport from the Accumulator to the Main Injector (MI) and optics improvements in Tevatron, Debuncher, and Accumulator. The electron cooler beam transport presented significant challenge for both the optics design and its commissioning.

2.1 Linear Optics with Coupling Between Degrees of Freedom

The major part of optics work has been focused on the linear optics problems. In this section we consider the fundamentals of betatron motion with coupled degrees of freedom. The significant fraction of Run II optics work has been based on this formalism and otherwise would hardly be possible. In particular the beam transport in the electron cooler (see Chap. 7) is completely x–y coupled, and the Tevatron lattice has significant coupling terms and the tune working point close to the difference resonance that it cannot be accurately described using the perturbation theory. The most of material is related to the x–y coupled motion. However, it can be directly applied to coupling of any two degrees of freedom. An extension to three degrees of freedom is straightforward and is not presented to keep text and equations compact.

V. Lebedev (✉) • V. Shiltsev • A. Valishev
Fermi National Accelerator Laboratory, PO Box 500, Batavia, IL 60510, USA
e-mail: val@fnal.gov; shiltsev@fnal.gov

V. Lebedev and V. Shiltsev (eds.), *Accelerator Physics at the Tevatron Collider*,
Particle Acceleration and Detection, DOI 10.1007/978-1-4939-0885-1_2,

First, we describe the equations of motion and notations. Second, we consider the relationship between eigenvectors, emittances, and the particle 4D ellipsoid in the phase space. Third, we consider the parameterization of particle motion based on an extension of the Mais–Ripken parameterization [1, 2] presented in [3]. Finally, we consider a perturbation theory for the case where the unperturbed motion is Hamiltonian.

2.1.1 Equations of Motion and Conditions of Symplecticity

In the absence of dissipative processes, the particle motion is Hamiltonian. For the linear motion the Hamiltonian is a second-order form of particle coordinates and momenta. For two-dimensional motion, it can be presented in the following matrix form:

$$H\left(x, p_x, y, p_y, s\right) = \mathbf{x}^{\mathrm{T}}\mathbf{H}\mathbf{x}, \tag{2.1}$$

where $\mathbf{x} = [x, p_x, y, p_y]^{\mathrm{T}}$, x and y are the particle coordinates, $p_x = x' - R\ y/2$ and $p_y = y' + R\ y/2$ are its canonical momenta,[1] $x' = dx/ds$ and $y' = dy/ds$ are the particle angles, s is the longitudinal coordinate (time coordinate), $R = eB_s/Pc$, B_s is the longitudinal magnetic field, and P is the total momentum of the reference particle. Following the standard procedure for obtaining the equations of motion [4],

$$\frac{dp_i}{dt} = -\frac{\partial H}{dx_i}, \quad \frac{dx_i}{dt} = \frac{\partial H}{dp_i}, \tag{2.2}$$

one comes to

$$\frac{d\mathbf{x}}{ds} = \mathbf{U}\mathbf{H}\mathbf{x}, \tag{2.3}$$

where

$$\mathbf{U} = \begin{bmatrix} 0 & 1 & 0 & 0 \\ -1 & 0 & 0 & 0 \\ 0 & 0 & 0 & 1 \\ 0 & 0 & -1 & 0 \end{bmatrix} \tag{2.4}$$

is the unit symplectic matrix. In the case of flat orbit, the Hamiltonian and the corresponding equations of motion are [2]

[1] Note that in practical optics calculations the difference between particle angles and their canonical momenta does not usually exist because most optics codes compute transfer matrices between points where the longitudinal magnetic fields are equal to zero.

$$\mathbf{H} = \begin{bmatrix} {K_x}^2 + k + \dfrac{R^2}{4} & 0 & N & -\dfrac{R}{2} \\ 0 & 1 & \dfrac{R}{2} & 0 \\ N & \dfrac{R}{2} & -k + \dfrac{R^2}{4} & 0 \\ -\dfrac{R}{2} & 0 & 0 & 1 \end{bmatrix}, \tag{2.5}$$

$$\begin{aligned} x'' + \left({K_x}^2 + k\right)x + \left(N - \frac{1}{2}R'\right)y - Ry' = 0 \quad , \\ y'' - ky + \left(N + \frac{1}{2}R'\right)x + Rx' = 0 \quad . \end{aligned} \tag{2.6}$$

Here $K_x = eB_y/Pc$, $k = eG/Pc$, $N = eG_s/Pc$, and B_y is the vertical component of the magnetic field; G and G_s are the normal and skew components of the magnetic field gradient (the skew component is obtained by +45° rotation around the s axis in the right-handed coordinate frame).

For any two solutions of Eq. (2.3), $\mathbf{x}_1(s)$ and $\mathbf{x}_2(s)$, one can write that

$$\frac{d}{ds}\left({\mathbf{x}_1}^{\mathrm{T}}\mathbf{U}\mathbf{x}_2\right) = \frac{d{\mathbf{x}_1}^{\mathrm{T}}}{ds}\ \mathbf{U}\mathbf{x}_2 + {\mathbf{x}_1}^{\mathrm{T}}\ \mathbf{U}\frac{d\mathbf{x}_2}{ds} = {\mathbf{x}_1}^{\mathrm{T}}\mathbf{H}^{\mathrm{T}}\mathbf{U}^{\mathrm{T}}\mathbf{U}\mathbf{x}_2 + {\mathbf{x}_1}^{\mathrm{T}}\mathbf{U}\mathbf{U}\mathbf{H}\mathbf{x}_2 = 0,$$

and, consequently,

$${\mathbf{x}_1}^{\mathrm{T}}\mathbf{U}\mathbf{x}_2 = \text{const}, \tag{2.7}$$

where the following properties of the unit symplectic matrix were employed: $\mathbf{U}^{\mathrm{T}}\mathbf{U} = \mathbf{I}$ and $\mathbf{U}\mathbf{U} = -\mathbf{I}$; $\mathbf{I}$ is the identity matrix. The integral of motion in Eq. (2.7) is called the Lagrange invariant.

Let us introduce the transfer matrix from coordinate 0 to coordinate s, $\mathbf{x} = \mathbf{M}(0, s)\mathbf{x}_0$. Taking into account that the invariant of Eq. (2.7) does not change during motion, we can write that

$${\mathbf{x}_1}^{\mathrm{T}}\mathbf{U}\mathbf{x}_2 = {\mathbf{x}_1}^{\mathrm{T}}\mathbf{M}(0,s)^{\mathrm{T}}\mathbf{U}\mathbf{M}(0,s)\mathbf{x}_2 = \text{const}.$$

As the above equation is satisfied for any $\mathbf{x}_1$ and $\mathbf{x}_2$, it yields

$$\mathbf{M}(0,s)^{\mathrm{T}}\mathbf{U}\mathbf{M}(0,s) = \mathbf{U}. \tag{2.8}$$

Equation (2.8) expresses the symplecticity condition for particle motion. It is equivalent to $n^2 = 16$ scalar equations, but taking into account that the matrix

$\mathbf{M}^{\mathrm{T}}\mathbf{U}\mathbf{M}$ is antisymmetric, only six ($(n^2-n)/2=6$) of these equations are independent [5]. Consequently, only 10 of 16 elements of the transfer matrix are independent. Thus, the symplecticity condition imposes more severe limitations than the Liouville's theorem [4], which imposes only one condition, $\det(\mathbf{M})=1$, and leaves 15 independent parameters.

Multiplying both sides of Eq. (2.8) by $\mathbf{U}$ on the left and by $\mathbf{M}^{-1}$ on the right, we obtain that the inverse of matrix $\mathbf{M}$ is

$$\mathbf{M}(0,s)^{-1} = -\mathbf{U}\mathbf{M}(0,s)^{\mathrm{T}}\mathbf{U}. \tag{2.9}$$

Then, multiplying Eq. (2.9) by $\mathbf{M}$ on the left and by $\mathbf{U}$ on the right, we obtain an alternative expression of symplecticity condition:

$$\mathbf{M}(0,s)\mathbf{U}\mathbf{M}(0,s)^{\mathrm{T}} = \mathbf{U}. \tag{2.10}$$

Note that Eqs. (2.9) and (2.10) are not related by matrix transposition.

2.1.2 Eigenvalues, Eigenvectors, and Condition of Motion Stability

Consider a circular accelerator with the one-turn transfer matrix $\mathbf{M}$. The transfer matrix has four eigenvalues, λ_i, and four corresponding eigenvectors, $\mathbf{v}_i$ ($i=1,2,3,4$):

$$\mathbf{M}\mathbf{v}_i = \lambda_i \mathbf{v}_i. \tag{2.11}$$

Then, the turn-by-turn particle motion can be presented in the following form:

$$\mathbf{x}_n = \sum_{i=1}^{4} \lambda_i^n c_i \mathbf{v}_i, \tag{2.12}$$

where c_i are the coefficients determined by particle initial coordinates.

Comparing the two equations below

$$\det(\mathbf{M}-\lambda\mathbf{I}) = \lambda^4 + \cdots + \det(\mathbf{M}) = \lambda^4 + \cdots + 1,$$
$$\det(\mathbf{M}-\lambda\mathbf{I}) = (\lambda-\lambda_1)(\lambda-\lambda_2)(\lambda-\lambda_3)(\lambda-\lambda_4) = \lambda^4 + \cdots + \lambda_1\lambda_2\lambda_3\lambda_4,$$

one obtains that the product of all eigenvalues is equal to 1:

$$\lambda_1\lambda_2\lambda_3\lambda_4 = 1. \tag{2.13}$$

Matrix $\mathbf{M}$ is a real matrix. Therefore, the complex conjugate of an eigenvalue and corresponding eigenvector are also an eigenvalue and eigenvector. As follows from Eq. (2.12) the motion stability requires $|\lambda_i| \le 1$. Combining that with the

requirement of Eq. (2.13), one obtains that the four eigenvalues split into two complex conjugate pairs confined to a unit circle, $|\lambda_i| = 1$. We denote them as λ_1, λ_1^*, λ_2, and λ_2^* and the corresponding eigenvectors as $\mathbf{v}_1$, $\mathbf{v}_1$*, $\mathbf{v}_2$, and $\mathbf{v}_2$*, where * denotes the complex conjugate value. Note that if any eigenvalue is equal to ± 1, its complex conjugate partner has the same value; consequently, the solution is degenerate and an infinitesimally small perturbation makes the system unstable.

For any two eigenvectors, the symplecticity condition of Eq. (2.8) yields the identity:

$$0 = \lambda_j \mathbf{v}_j{}^{\mathrm{T}} \mathbf{U}(\mathbf{M}\mathbf{v}_i - \lambda_i \mathbf{v}_i) = \left(\mathbf{M}\mathbf{v}_j\right)^{\mathrm{T}} \mathbf{U}\mathbf{M}\mathbf{v}_i - \lambda_j \mathbf{v}_j{}^{\mathrm{T}} \mathbf{U}\lambda_i \mathbf{v}_i = \left(1 - \lambda_j \lambda_i\right) \mathbf{v}_j{}^{\mathrm{T}} \mathbf{U}\mathbf{v}_i,$$

which results in that the product $\mathbf{v}_j{}^{\mathrm{T}}\mathbf{U}\mathbf{v}_i$ can be different from zero only if $\mathbf{v}_i$ and $\mathbf{v}_j$ represent a complex conjugate pair. The product $\mathbf{v}_j{}^{+}\mathbf{U}\mathbf{v}_i$ is purely imaginary, indeed:

$$\left(\mathbf{v}^{+}\mathbf{U}\mathbf{v}\right)^{*} = \left(\mathbf{v}^{+}\mathbf{U}\mathbf{v}\right)^{+} = \mathbf{v}^{+}\mathbf{U}^{+}\mathbf{v} = -\mathbf{v}^{+}\mathbf{U}\mathbf{v},$$

where $\mathbf{v}^{+} = \mathbf{v}^{*\mathrm{T}}$ denotes the Hermitian conjugate, and we took into account that the transpose of a scalar is equal to itself. That allows us to introduce the symplectic orthogonality conditions:

$$\begin{aligned} \mathbf{v}_1{}^{+}\mathbf{U}\mathbf{v}_1 &= -2i, \quad & \mathbf{v}_2{}^{+}\mathbf{U}\mathbf{v}_2 &= -2i, \\ \mathbf{v}_1{}^{T}\mathbf{U}\mathbf{v}_1 &= 0, & \mathbf{v}_2{}^{T}\mathbf{U}\mathbf{v}_2 &= 0, \\ \mathbf{v}_2{}^{T}\mathbf{U}\mathbf{v}_1 &= 0, & \mathbf{v}_2{}^{+}\mathbf{U}\mathbf{v}_1 &= 0. \end{aligned} \tag{2.14}$$

Other combinations can be obtained by applying the transposition and/or the complex conjugation to Eq. (2.14). Note that the sign choice in the two top equations determines which of two vectors in each complex conjugate pair is the primary vector (see Sect. 2.1.5). The normalization value is chosen to make the matrix $\mathbf{V}$ introduced in the next section symplectic. Similarly as for the transfer matrix elements, there are only six independent real scalar equations among Eq. (2.14). Note that the two equations in the second line are identities because $\mathbf{a}^{+}\,\mathbf{U}\,\mathbf{a} = 0$ for any $\mathbf{a}$.

2.1.3 *Mode Emittances and Emittance Ellipsoid in 4D Phase Space*

The turn-by-turn particle positions and angles can be represented as a linear combination of four independent solutions,

$$\begin{aligned}\mathbf{x} &= \mathrm{Re}\left(A_1 \mathrm{e}^{-\mathrm{i}\psi_1}\mathbf{v}_1 + A_2 \mathrm{e}^{-\mathrm{i}\psi_2}\mathbf{v}_2\right) \\ &= A_1(\mathbf{v}_1{}' \cos\psi_1 + \mathbf{v}_1{}'' \sin\psi_1) + A_2(\mathbf{v}_2{}' \cos\psi_2 + \mathbf{v}_2{}'' \sin\psi_2),\end{aligned} \tag{2.15}$$

where four real parameters, A_1, A_2, ψ_1, and ψ_2, represent the betatron amplitudes and phases. The amplitudes remain constant in the course of betatron motion, while the phases are incremented after each turn.

Let us introduce the following real matrix:

$$\mathbf{V} = [\mathbf{v}_1{}', -\mathbf{v}_1{}'', \mathbf{v}_2{}', -\mathbf{v}_2{}'']. \tag{2.16}$$

This allows one to rewrite Eq. (2.15) in the compact form

$$\mathbf{x} = \mathbf{V}\mathbf{A}\boldsymbol{\xi}_A, \tag{2.17}$$

where the amplitude matrix $\mathbf{A}$ is

$$\mathbf{A} = \begin{bmatrix} A_1 & 0 & 0 & 0 \\ 0 & A_1 & 0 & 0 \\ 0 & 0 & A_2 & 0 \\ 0 & 0 & 0 & A_2 \end{bmatrix} \equiv \mathrm{diag}(A_1, A_1, A_2, A_2), \tag{2.18}$$

and

$$\boldsymbol{\xi}_A = \begin{bmatrix} \cos\psi_1 \\ -\sin\psi_1 \\ \cos\psi_2 \\ -\sin\psi_2 \end{bmatrix}. \tag{2.19}$$

Applying the orthogonality conditions given by Eq. (2.14), one can prove that matrix $\mathbf{V}$ is a symplectic matrix. It can be seen explicitly as follows:

$$\mathbf{V}^{\mathrm{T}}\mathbf{U}\mathbf{V} = \left[\frac{\mathbf{v}_1 + \mathbf{v}_1{}^*}{2}, -\frac{\mathbf{v}_1 - \mathbf{v}_1{}^*}{2i}, \frac{\mathbf{v}_2 + \mathbf{v}_2{}^*}{2}, -\frac{\mathbf{v}_2 - \mathbf{v}_2{}^*}{2i}\right]^{\mathrm{T}}$$
$$\mathbf{U}\left[\frac{\mathbf{v}_1 + \mathbf{v}_1{}^*}{2}, -\frac{\mathbf{v}_1 - \mathbf{v}_1{}^*}{2i}, \frac{\mathbf{v}_2 + \mathbf{v}_2{}^*}{2}, -\frac{\mathbf{v}_2 - \mathbf{v}_2{}^*}{2i}\right] = \mathbf{U}.$$

Here we took into account that every matrix element in matrix $\hat{\mathbf{V}}^{\mathrm{T}}\mathbf{U}\hat{\mathbf{V}}$ can be calculated using vector multiplication of Eq. (2.14).

Let us consider an ensemble of particles, whose motion at the beginning of the lattice (or any other point of a ring) is contained in a 4D ellipsoid. A 3D surface of this ellipsoid is determined by particles with extreme betatron amplitudes. For any

of these particles, Eq. (2.17) describes the 2D subspace of single-particle motion, which is a subspace of the 3D surface of the ellipsoid, described by the bilinear form

$$\mathbf{x}^{\mathrm{T}}\boldsymbol{\Xi}\mathbf{x} = 1. \tag{2.20}$$

This ellipsoid confines the motion of all particles. To describe a 3D surface, in addition to parameters ψ_1 and ψ_2 of Eq. (2.19), we introduce the third parameter ψ_3 so that the vector $\boldsymbol{\xi}$ would belong to a 3D sphere with a unit radius, according to the equation

$$(\boldsymbol{\xi}, \boldsymbol{\xi}) = 1, \tag{2.21}$$

where

$$\boldsymbol{\xi} = \begin{bmatrix} \cos\psi_1 \cos\psi_3 \\ -\sin\psi_1 \cos\psi_3 \\ \cos\psi_2 \sin\psi_3 \\ -\sin\psi_2 \sin\psi_3 \end{bmatrix}. \tag{2.22}$$

Then, we can rewrite Eq. (2.17) in the following form:

$$\mathbf{x} = \mathbf{V}\mathbf{A}\boldsymbol{\xi} \tag{2.23}$$

which describes a 3D subspace confining all particles of the beam (water-bag particle distribution). In other words we can consider that the amplitudes of the boundary particles are parameterized by ψ_3 ($A_1 \to A_1 \cos\psi_3, A_2 \to A_2 \sin\psi_3$), so that we would obtain a 4D ellipsoid.

Expressing $\boldsymbol{\xi}$ from Eq. (2.23) and substituting it into Eq. (2.21), one obtains the quadratic form describing a 4D ellipsoid containing all particles:

$$\mathbf{x}^{\mathrm{T}}\left((\mathbf{V}\mathbf{A})^{-1}\right)^{\mathrm{T}}(\mathbf{V}\mathbf{A})^{-1}\mathbf{x} = 1. \tag{2.24}$$

Comparing Eqs. (2.20) and (2.24) and using Eq. (2.9) for matrix inversion, one can express the bilinear form, $\boldsymbol{\Xi}$, as follows:

$$\boldsymbol{\Xi} = \mathbf{U}\mathbf{V}\hat{\boldsymbol{\Xi}}\mathbf{V}^{\mathrm{T}}\mathbf{U}^{\mathrm{T}}, \tag{2.25}$$

where $\hat{\boldsymbol{\Xi}} = \mathbf{A}^{-1}\mathbf{A}^{-1} = \mathrm{diag}\left(A_1{}^{-2}, A_1{}^{-2}, A_2{}^{-2}, A_2{}^{-2}\right)$ is a diagonal matrix depending on two amplitudes A_1 and A_2, and we took into account that matrices $\mathbf{A}^{-1}$ and $\mathbf{U}$ commute. Inversion of Eq. (2.25) yields

$$\hat{\boldsymbol{\Xi}} = \mathbf{V}^{\mathrm{T}}\boldsymbol{\Xi}\mathbf{V}, \tag{2.26}$$

i.e., a symplectic transform $\mathbf{V}$ reduces matrix $\boldsymbol{\Xi}$ to its diagonal form.

To determine the beam emittance (volume of the occupied 4D phase space) described by Eq. (2.20), we note that due to symplecticity $\det(\mathbf{V}) = 1$. Consequently, the coordinate transform $\mathbf{x} = \mathbf{V}\mathbf{x}'$ corresponding to Eq. (2.26) does not change the ellipsoid volume. Then, in the new coordinate frame, the 3D ellipsoid enclosing the total 4D phase space of the beam is described by the following equation:

$$\hat{\Xi}_{11}x'^2 + \hat{\Xi}_{22}p'^2 + \hat{\Xi}_{33}y'^2 + \hat{\Xi}_{44}y'^2 = 1.$$

It is natural to define the beam emittance as a product of the ellipsoid semiaxes (omitting the factor $\pi^2/2$ correcting for the real 4D volume of the ellipsoid) so that

$$\varepsilon_{4D} = \frac{1}{\sqrt{\hat{\Xi}_{11}\hat{\Xi}_{22}\hat{\Xi}_{33}\hat{\Xi}_{44}}} = \frac{1}{\sqrt{\det(\hat{\Xi})}} = {A_1}^2{A_2}^2. \tag{2.27}$$

Thus, the squares of amplitudes A_1 and A_2 can be considered as 2D emittances ε_1 and ε_2 corresponding to the eigenvectors $\mathbf{v}_1$ and $\mathbf{v}_2$. Their product is equal to the total 4D emittance: $\varepsilon_1\varepsilon_2 = \varepsilon_{4D}$. We will call them the mode emittances. Consequently, one can write matrix $\hat{\Xi}$ as

$$\hat{\Xi} = \mathrm{diag}\left({\varepsilon_1}^{-1}, {\varepsilon_1}^{-1}, {\varepsilon_2}^{-1}, {\varepsilon_2}^{-1}\right). \tag{2.28}$$

2.1.4 Eigenvectors and Particle Phase Space Ellipsoid

Similarly to the one-dimensional case, the particle ellipsoid shape, described by matrix Ξ, determines the mode emittances ε_1 and ε_2 and the eigenvectors $\mathbf{v}_1$ and $\mathbf{v}_2$. In this case the mode emittances are reciprocal to the roots of the following characteristic equation:

$$\det(\Xi - i\lambda\mathbf{U}) = 0. \tag{2.29}$$

One can prove the above using Eq. (2.25) as follows:

$$\begin{aligned}\det(\Xi - i\lambda\mathbf{U}) &= \det\left(\mathbf{U}\mathbf{V}\hat{\Xi}\mathbf{V}^{\mathrm{T}}\mathbf{U}^{\mathrm{T}} - i\lambda\mathbf{U}\right) = \det\left(\hat{\Xi} - i\lambda\mathbf{U}^{\mathrm{T}}\mathbf{V}^{\mathrm{T}}\mathbf{U}\mathbf{V}\mathbf{U}\right)\\ &= \det\left(\hat{\Xi} - i\lambda\mathbf{U}\right) = \left(\frac{1}{{\varepsilon_1}^2} - \lambda^2\right)\left(\frac{1}{{\varepsilon_2}^2} - \lambda^2\right) = 0.\end{aligned} \tag{2.30}$$

Knowing the mode emittances and, consequently, $\hat{\Xi}$, one can obtain from Eq. (2.25) a system of linear equations for matrix $\mathbf{V}$:

$$\boldsymbol{\Xi}\mathbf{V}\mathbf{U} = \mathbf{U}\mathbf{V}\hat{\boldsymbol{\Xi}}. \tag{2.31}$$

Multiplying the above equation by u_l, one obtains two equations for the eigenvectors:

$$\left(\boldsymbol{\Xi} - \frac{i}{\varepsilon_l}\mathbf{U}\right)\mathbf{v}_l = 0, \tag{2.32}$$

where $l = 1, 2$, and

$$\mathbf{u}_1 = \begin{bmatrix} 1 \\ -i \\ 0 \\ 0 \end{bmatrix}, \quad \mathbf{u}_2 = \begin{bmatrix} 0 \\ 0 \\ 1 \\ -i \end{bmatrix}. \tag{2.33}$$

We also took into account that $\mathbf{V}\mathbf{u}_l = \mathbf{v}_l$, $\mathbf{U}\mathbf{u}_l = -i\mathbf{u}_l$, and $\boldsymbol{\Xi}'\mathbf{u}_l = \frac{1}{\varepsilon_l}\mathbf{u}_l$.

Taking into account Eq. (2.20) a Gaussian distribution function for coupled beam motion can be written in the following form:

$$f(\mathbf{x}) = \frac{1}{4\pi^2\varepsilon_1\varepsilon_2}\,\exp\left(-\frac{1}{2}\mathbf{x}^{\mathrm{T}}\boldsymbol{\Xi}\mathbf{x}\right). \tag{2.34}$$

Then, the second-order moments of the distribution function are

$$\Sigma_{ij} \equiv \overline{x_i x_j} = \int x_i x_j f(\mathbf{x}) dx^4 = \frac{1}{4\pi^2\varepsilon_1\varepsilon_2}\int x_i x_j\,\exp\left(-\frac{1}{2}\mathbf{x}^{\mathrm{T}}\boldsymbol{\Xi}\mathbf{x}\right) dx^4. \tag{2.35}$$

To carry out the integration, one can perform a coordinate transform, $\mathbf{y} = \mathbf{V}^{-1}\mathbf{x}$, which reduces matrix $\boldsymbol{\Xi}$ to its diagonal form. Taking into account that

$$\frac{1}{4\pi^2\varepsilon_1\varepsilon_2}\int y_i y_j dy^4\,\exp\left(-\frac{1}{2}\mathbf{y}^{\mathrm{T}}\hat{\boldsymbol{\Xi}}\mathbf{y}\right) = [\mathrm{diag}(\varepsilon_1, \varepsilon_1, \varepsilon_2, \varepsilon_2)]_{ij} \equiv \hat{\boldsymbol{\Sigma}}_{ij}, \tag{2.36}$$

one obtains that the matrix of the second-order moments is

$$\boldsymbol{\Sigma} = \mathbf{V}\hat{\boldsymbol{\Sigma}}\,\mathbf{V}^{\mathrm{T}}. \tag{2.37}$$

Using Eqs. (2.25) and (2.37), one can easily prove that matrix $\boldsymbol{\Sigma}$ is the inverse of matrix $\boldsymbol{\Xi}$. Consequently, a symplectic transform $\mathbf{V}\mathbf{U}$ reduces matrix $\boldsymbol{\Sigma}$ to its diagonal form. Applying a similar scheme as above for obtaining emittances and eigenvectors from matrix $\boldsymbol{\Xi}$, one finds that the mode emittances ε_1 and ε_2 can be computed from matrix $\boldsymbol{\Sigma}$ as roots of its characteristic equation,

$$\det(\boldsymbol{\Sigma}\mathbf{U} + i\lambda\mathbf{I}) = 0, \quad \varepsilon_l = \lambda_l, \tag{2.38}$$

while the equations for the eigenvectors are

$$(\mathbf{\Sigma U} + i\varepsilon_l \mathbf{I})\mathbf{v}_l = 0. \tag{2.39}$$

It also follows from Eq. (2.37) that the total beam emittance is equal to

$$\varepsilon_{4D} = \varepsilon_1 \varepsilon_2 = \sqrt{\det(\mathbf{\Sigma})}. \tag{2.40}$$

Taking into account that the beam motion from point s to point s' results in the matrix $\mathbf{\Xi}$ transformation so that $\mathbf{\Xi}(s') = \mathbf{M}(s,s')^{\mathrm{T}}\mathbf{\Xi}(s)\mathbf{M}(s,s')$ and using Eq. (2.29) and the motion symplecticity, one can easily prove that the mode emittances ε_1 and ε_2 are the motion invariants, i.e., there is no configuration of linear electric and magnetic fields which can change them. Consequently, each mode emittance is bound to the corresponding betatron mode. If the beamline is built so that the motion is decoupled at some point, then the mode emittances coincide with conventional horizontal and vertical emittances.

2.1.5 Beta-Functions of Coupled Motion

Employing the previously introduced notation, one can describe a single-particle phase-space trajectory along the beam orbit as

$$\begin{aligned}\mathbf{x}(s) &= \mathbf{M}(0,s)\mathrm{Re}\left(\sqrt{2I_1}\mathbf{v}_1 \mathrm{e}^{-i\psi_1} + \sqrt{2I_2}\mathbf{v}_2 \mathrm{e}^{-i\psi_2}\right) \\ &= \mathrm{Re}\left(\sqrt{2I_1}\mathbf{v}_1(s)\mathrm{e}^{-i(\psi_1+\mu_1(s))} + \sqrt{2I_2}\mathbf{v}_2(s)\mathrm{e}^{-i(\psi_2+\mu_2(s))}\right),\end{aligned} \tag{2.41}$$

where the vectors $\mathbf{v}_1(s) \equiv \mathrm{e}^{i\mu_1(s)}\mathbf{M}(0,s)\mathbf{v}_1$ and $\mathbf{v}_2(s) \equiv \mathrm{e}^{i\mu_2(s)}\mathbf{M}(0,s)\mathbf{v}_2$ are the eigenvectors of the matrix $\mathbf{M}(0,s)\mathbf{M}\mathbf{M}(0,s)^{-1}$, ψ_1 and ψ_2 are the initial phases of betatron motion and I_1 and I_2 are the corresponding actions, and $\mathbf{M} = \mathbf{M}(0,L)$ is the transfer matrix for the entire ring. The terms $\mathrm{e}^{-i\mu_1(s)}$ and $\mathrm{e}^{-i\mu_2(s)}$ are introduced to bring the eigenvectors to the following form:

$$\mathbf{v}_1(s) = \begin{bmatrix} \sqrt{\beta_{1x}(s)} \\ -\dfrac{iu_1(s) + \alpha_{1x}(s)}{\sqrt{\beta_{1x}(s)}} \\ \sqrt{\beta_{1y}(s)}\mathrm{e}^{i\nu_1(s)} \\ -\dfrac{iu_2(s) + \alpha_{1y}(s)}{\sqrt{\beta_{1y}(s)}}\mathrm{e}^{i\nu_1(s)} \end{bmatrix}, \quad \mathbf{v}_2(s) = \begin{bmatrix} \sqrt{\beta_{2x}(s)}\mathrm{e}^{i\nu_2(s)} \\ -\dfrac{iu_3(s) + \alpha_{2x}(s)}{\sqrt{\beta_{2x}(s)}}\mathrm{e}^{i\nu_2(s)} \\ \sqrt{\beta_{2y}(s)} \\ -\dfrac{iu_4(s) + \alpha_{2y}(s)}{\sqrt{\beta_{2y}(s)}} \end{bmatrix}, \tag{2.42}$$

so that $\mu_1(s)$ and $\mu_2(s)$ would be the phase advances of betatron motion. Here $\beta_{1x}(s)$, $\beta_{1y}(s)$, $\beta_{2x}(s)$, and $\beta_{2y}(s)$ are the beta-functions; $\alpha_{1x}(s)$, $\alpha_{1y}(s)$, $\alpha_{2x}(s)$, and $\alpha_{2y}(s)$ are

the alpha-functions which, as will be shown in the next section, coincide with the beta-functions' negative half-derivatives at regions with zero longitudinal magnetic field; and six real functions $u_1(s)$, $u_2(s)$, $u_3(s)$, $u_4(s)$, $v_1(s)$, and $v_2(s)$ are determined by the orthogonality conditions of Eq. (2.14). Below we will be omitting their dependence on s where it does not cause an ambiguity. Two eigenvectors $\mathbf{v}_1$ and $\mathbf{v}_2$ were chosen out of two pairs of complex conjugate eigenvectors by selecting u_1 and u_4 to be positive.

The first orthogonality condition of Eq. (2.14),

$$(\mathbf{v}_1{}^{+}\mathbf{U}\mathbf{v}_1) = -2i(u_1 + u_2) = -2i,$$

yields $u_1 = 1 - u_2$, and similarly for the second eigenvector, $u_4 = 1 - u_3$. The next two equations, $\mathbf{v}_1{}^{\mathrm{T}}\mathbf{U}\mathbf{v}_1 = 0$ and $\mathbf{v}_2{}^{\mathrm{T}}\mathbf{U}\mathbf{v}_2 = 0$, are identities.

Taking into account the above relations for u_1 and u_4, the remaining two nontrivial orthogonality conditions can be written as follows:

$$\begin{aligned}(\mathbf{v}_2{}^{+}\mathbf{U}\mathbf{v}_1) = &-\left(\sqrt{\frac{\beta_{2x}}{\beta_{1x}}}\left[i(1-u_2)+\alpha_{1x}\right] + \sqrt{\frac{\beta_{1x}}{\beta_{2x}}}\left[iu_3 - \alpha_{2x}\right]\right)\mathrm{e}^{-i\nu_2} \\ &-\left(\sqrt{\frac{\beta_{1y}}{\beta_{2y}}}\left[i(1-u_3)-\alpha_{2y}\right] + \sqrt{\frac{\beta_{2y}}{\beta_{1y}}}\left[iu_2 + \alpha_{1y}\right]\right)\mathrm{e}^{i\nu_1} = 0,\end{aligned} \tag{2.43}$$

$$\begin{aligned}(\mathbf{v}_2{}^{\mathrm{T}}\mathbf{U}\mathbf{v}_1) = &-\left(\sqrt{\frac{\beta_{2x}}{\beta_{1x}}}\left[i(1-u_2)+\alpha_{1x}\right] - \sqrt{\frac{\beta_{1x}}{\beta_{2x}}}\left[iu_3 + \alpha_{2x}\right]\right)\mathrm{e}^{i\nu_2} \\ &-\left(\sqrt{\frac{\beta_{1y}}{\beta_{2y}}}\left[i(u_3-1)-\alpha_{2y}\right] + \sqrt{\frac{\beta_{2y}}{\beta_{1y}}}\left[iu_2 + \alpha_{1y}\right]\right)\mathrm{e}^{i\nu_1} = 0.\end{aligned} \tag{2.44}$$

Multiplying both terms in Eqs. (2.43) and (2.44) by their complex conjugate values, one obtains

$$\begin{aligned}A_x{}^2 + \left(\kappa_x(1-u_2) + \kappa_x{}^{-1}u_3\right)\big)^2 &= A_y{}^2 + \left(\kappa_y(1-u_3) + \kappa_y{}^{-1}u_2\right)^2, \\ A_x{}^2 + \left(\kappa_x(1-u_2) - \kappa_x{}^{-1}u_3\right)\big)^2 &= A_y{}^2 + \left(\kappa_y(1-u_3) - \kappa_y{}^{-1}u_2\right)^2,\end{aligned} \tag{2.45}$$

where

$$\begin{aligned} A_x &= \kappa_x \alpha_{1x} - {\kappa_x}^{-1} \alpha_{2x}, \\ A_y &= \kappa_y \alpha_{2y} - {\kappa_y}^{-1} \alpha_{1y}, \\ \kappa_x &= \sqrt{\frac{\beta_{2x}}{\beta_{1x}}}, \quad \kappa_y = \sqrt{\frac{\beta_{1y}}{\beta_{2y}}}. \end{aligned} \tag{2.46}$$

Subtracting Eq. (2.45) yields $u_2 = u_3$. Substituting $u_2 = u_3 = u$ into the first equation of Eq. (2.45), one obtains the following expression for u:

$$u = \frac{-{\kappa_x}^2 {\kappa_y}^2 \pm \sqrt{{\kappa_x}^2 {\kappa_y}^2 \left(1 + \frac{{A_x}^2 - {A_y}^2}{{\kappa_x}^2 - {\kappa_y}^2}\left(1 - {\kappa_x}^2 {\kappa_y}^2\right)\right)}}{1 - {\kappa_x}^2 {\kappa_y}^2}. \tag{2.47}$$

By definition u_k ($k = 1, \ldots 4$) are real functions[2] and u_1 and u_4 are positive. That sets a constraint for possible values of beta- and alpha-functions,

$$\frac{{A_x}^2 - {A_y}^2}{{\kappa_x}^2 - {\kappa_y}^2}\left(1 - {\kappa_x}^2 {\kappa_y}^2\right) \geq -1, \tag{2.48}$$

and a constraint on a value of u, $u \leq 1$ (see also Sect. 2.1.6).

Knowing u makes it easy to find $\nu_1 + \nu_2$ and $\nu_1 - \nu_2$ from Eqs. (2.43) and (2.44):

$$\begin{aligned} \mathrm{e}^{i\nu_+} \equiv \mathrm{e}^{i(\nu_1+\nu_2)} &= \frac{A_x + i\left(\kappa_x(1-u) + {\kappa_x}^{-1}u\right)}{A_y - i\left(\kappa_y(1-u) + {\kappa_y}^{-1}u\right)}, \\ \mathrm{e}^{i\nu_-} \equiv \mathrm{e}^{i(\nu_1-\nu_2)} &= \frac{A_x + i\left(\kappa_x(1-u) - {\kappa_x}^{-1}u\right)}{A_y + i\left(\kappa_y(1-u) - {\kappa_y}^{-1}u\right)}, \end{aligned} \tag{2.49}$$

and, consequently, ν_1 and ν_2:

$$\begin{aligned} \nu_1 &= \frac{1}{2}(\nu_+ + \nu_-) + \pi(n+m), \\ \nu_2 &= \frac{1}{2}(\nu_+ - \nu_-) + \pi(n-m). \end{aligned} \tag{2.50}$$

Here n and m are arbitrary integers. Equation (2.49) results in that ν_- and ν_+ are determined modulo 2π which, consequently, yields that ν_1 and ν_2 are determined modulo π (see Eq. (2.50)) resulting in additional solutions. Actually there are only two independent solutions for ν_1 and ν_2. The first one corresponds to the case when

[2] Equation (2.47) also demonstrates that if beta- and alpha-functions are chosen incorrectly, such that the value of the discriminant is negative, u becomes imaginary, thus redetermining the alpha-functions.

both n and m have the same parity, which is equivalent to $m+n=m-n=0$. The second one corresponds to different parity of m and n, which is equivalent to $m+n=m-n=1$. Thus, in a general case, one has four independent solutions for u and ν_1 and ν_2 set by symplecticity conditions: two solutions for u and two solutions for ν_1 and ν_2 for each u.

Finally, we can express the eigenvectors in the following form:

$$\mathbf{v}_1 = \begin{bmatrix} \sqrt{\beta_{1x}} \\ -\dfrac{i(1-u)+\alpha_{1x}}{\sqrt{\beta_{1x}}} \\ \sqrt{\beta_{1y}}\,e^{i\nu_1} \\ -\dfrac{iu+\alpha_{1y}}{\sqrt{\beta_{1y}}}\,e^{i\nu_1} \end{bmatrix}, \quad \mathbf{v}_2 = \begin{bmatrix} \sqrt{\beta_{2x}}\,e^{i\nu_2} \\ -\dfrac{iu+\alpha_{2x}}{\sqrt{\beta_{2x}}}\,e^{i\nu_2} \\ \sqrt{\beta_{2y}} \\ -\dfrac{i(1-u)+\alpha_{2y}}{\sqrt{\beta_{2y}}} \end{bmatrix}. \tag{2.51}$$

That yields the following expression for matrix $\mathbf{V}$ (see Eq. (2.16)):

$$\mathbf{V} = \begin{bmatrix} \sqrt{\beta_{1x}} & 0 & \sqrt{\beta_{2x}}\cos\nu_2 & -\sqrt{\beta_{2x}}\sin\nu_2 \\ -\dfrac{\alpha_{1x}}{\sqrt{\beta_{1x}}} & \dfrac{1-u}{\sqrt{\beta_{1x}}} & \dfrac{u\sin\nu_2-\alpha_{2x}\cos\nu_2}{\sqrt{\beta_{2x}}} & \dfrac{u\cos\nu_2+\alpha_{2x}\sin\nu_2}{\sqrt{\beta_{2x}}} \\ \sqrt{\beta_{1y}}\cos\nu_1 & -\sqrt{\beta_{1y}}\sin\nu_1 & \sqrt{\beta_{2y}} & 0 \\ \dfrac{u\sin\nu_1-\alpha_{1y}\cos\nu_1}{\sqrt{\beta_{1y}}} & \dfrac{u\cos\nu_1+\alpha_{1y}\sin\nu_1}{\sqrt{\beta_{1y}}} & -\dfrac{\alpha_{2y}}{\sqrt{\beta_{2y}}} & \dfrac{1-u}{\sqrt{\beta_{2y}}} \end{bmatrix}. \tag{2.52}$$

Below we will call eleven functions, $\beta_{1x}(s)$, $\beta_{1y}(s)$, $\beta_{2x}(s)$, $\beta_{2y}(s)$, $\alpha_{1x}(s)$, $\alpha_{1y}(s)$, $\alpha_{2x}(s)$, $\alpha_{2y}(s)$, $u(s)$, $\nu_1(s)$, and $\nu_2(s)$, the generalized Twiss functions. Only eight of them are independent. Other three can be determined from the symplecticity conditions. Although for known eigenvectors the Twiss parameters can be determined uniquely, it is not the case if we know only alpha- and beta-functions. In this case an application of symplecticity conditions leaves four independent solutions for the eigenvectors. Two of them are related to the sign choice for u in Eq. (2.47), and other two (for each choice of u) are related to uncertainty of ν_1 and ν_2 in Eq. (2.50). The latter is related to the fact that the mirror reflection with respect to the x or y axis does not change β's and α's but changes the relative signs for the x and y components of the eigenvectors, with subsequent change of ν_1 and ν_2 by π. It can also be achieved by a change of the coupling sign (simultaneous sign change for gradients of all skew quads and magnetic fields of all solenoids), which does not change the beta-functions but does change the ν-functions by π. To choose a unique solution for the eigenvectors, one needs to know which of the two choices for u and ν_1 (or ν_2) needs to be taken in addition to the alpha- and beta-functions.

In the case of weak coupling, one should normally choose $\mathbf{v}_1$ as the eigenvector, which mainly relates to the horizontal motion, and $\mathbf{v}_2$ to the vertical motion. In the case of strong coupling, the choice is arbitrary. As can be seen from Eq. (2.51), in

determining beta- and alpha-functions, swapping two eigenvectors causes the following redefinitions: $\beta_{1x} \leftrightarrow \beta_{2x}$, $\beta_{1y} \leftrightarrow \beta_{2y}$, $\alpha_{1x} \leftrightarrow \alpha_{2x}$, $\alpha_{1y} \leftrightarrow \alpha_{2y}$, $u \to 1-u$, $\nu_1 \to -\nu_2$, and $\nu_2 \to -\nu_1$.

2.1.6 Derivatives of the Tunes and Beta-Functions

Let us consider the relations between the beta- and alpha-functions and the beta-functions and the betatron phase advances. A differential trajectory displacement related to the first eigenvector can be expressed as follows:

$$x(s+ds)=x(s)+x'(s)ds=x(s)+\left(p_x(s)+\frac{R}{2}y\right)ds$$
$$=\sqrt{2I_1}\mathrm{Re}\left(\left(\sqrt{\beta_{1x}(s)}+\left[-\frac{i(1-u(s))+\alpha_{1x}(s)}{\sqrt{\beta_{1x}(s)}}+\frac{R}{2}\sqrt{\beta_{1y}(s)}\,\mathrm{e}^{i\nu_1(s)}\right]ds\right)\mathrm{e}^{-i(\mu_1(s)+\psi_1)}\right). \tag{2.53}$$

Alternatively, one can express particle position through the beta-functions at the new coordinate $s + ds$:

$$x(s+ds) = \mathrm{Re}\left(\sqrt{2I_1\beta_x(s+ds)}\mathrm{e}^{-i(\mu_1(s+ds)+\psi)}\right)$$
$$= \sqrt{2I_1}\mathrm{Re}\left(\left[\sqrt{\beta_{1x}(s)}+\frac{d\beta_{1x}}{2\sqrt{\beta_{1x}(s)}}-i\sqrt{\beta_{1x}(s)}d\mu\right]\mathrm{e}^{-i(\mu_1(s)+\psi)}\right). \tag{2.54}$$

Comparing both the imaginary and real parts of Eqs. (2.53) and (2.54), one obtains

$$\frac{d\beta_{1x}}{ds} = -2\alpha_{1x} + R\sqrt{\beta_{1x}\beta_{1y}}\cos\nu_1,$$
$$\frac{d\mu_1}{ds} = \frac{1-u}{\beta_{1x}} - \frac{R}{2}\sqrt{\frac{\beta_{1y}}{\beta_{1x}}}\sin\nu_1. \tag{2.55}$$

Similarly, one can write down equivalent expressions for the vertical displacement,

$$y(s+ds)=y(s)+y'(s)ds=y(s)+\left(p_y(s)-\frac{R}{2}x\right)ds$$

$$=\sqrt{2I_1}\mathrm{Re}\left(\left(\sqrt{\beta_{1y}(s)}\mathrm{e}^{i\nu_1(s)}-\left[\frac{iu(s)+\alpha_{1y}(s)}{\sqrt{\beta_{1y}(s)}}\,\mathrm{e}^{i\nu_1(s)}+\frac{R}{2}\sqrt{\beta_{1x}(s)}\right]ds\right)\mathrm{e}^{-i(\mu_1(s)+\psi_1)}\right),$$

and

$$y(s+ds)=\sqrt{2I_1}\mathrm{Re}\left(\left[\sqrt{\beta_{1y}(s)}+\frac{d\beta_{1y}}{2\sqrt{\beta_{1y}(s)}}+i\sqrt{\beta_{1y}(s)}(d\nu_1-d\mu_1)\right]\mathrm{e}^{-i(\mu_1(s)+\psi-\nu_1(s))}\right),$$

which yields

$$\begin{aligned}\frac{d\beta_{1y}}{ds}&=-2\alpha_{1y}-R\sqrt{\beta_{1x}\beta_{1y}}\cos\nu_1,\\ \frac{d\mu_1}{ds}-\frac{d\nu_1}{ds}&=\frac{u}{\beta_{1y}}+\frac{R}{2}\sqrt{\frac{\beta_{1x}}{\beta_{1y}}}\sin\nu_1.\end{aligned}\tag{2.56}$$

Similar calculations carried out for the second eigenvector yield

$$\begin{aligned}\frac{d\beta_{2y}}{ds}&=-2\alpha_{2y}-R\sqrt{\beta_{2x}\beta_{2y}}\cos\nu_2,\\ \frac{d\mu_2}{ds}&=\frac{1-u}{\beta_{2y}}+\frac{R}{2}\sqrt{\frac{\beta_{2x}}{\beta_{2y}}}\sin\nu_2,\\ \frac{d\beta_{2x}}{ds}&=-2\alpha_{2x}+R\sqrt{\beta_{2x}\beta_{2y}}\cos\nu_2,\\ \frac{d\mu_2}{ds}-\frac{d\nu_2}{ds}&=\frac{u}{\beta_{2x}}-\frac{R}{2}\sqrt{\frac{\beta_{2y}}{\beta_{2x}}}\sin\nu_2.\end{aligned}\tag{2.57}$$

One can see that in the absence of longitudinal magnetic field, the alpha- and beta-functions are related the same way as for the uncoupled case ($\alpha=-(d\beta/ds)/2$) and the derivatives of the phase advances $d\mu_1/ds$ and $d\mu_2/ds$ are proportional to $(1-u)$ and are positive. That explains the selection rule for the eigenvectors formulated in Sect. 4.1.5 which requires u_1 and u_4 being positive ($u_1=u_4=1-u\geq 0$). Note that there is no formal requirement for $d(\mu_1+\nu_1)/ds$

and $d(\mu_2+\nu_2)/ds$ being also positive, and therefore u can be negative,[3] while in the majority of practical cases, it belongs to the [0, 1] interval.

2.1.7 Representation of Transfer Matrix and Second-Order Moments in Terms of Generalized Twiss Functions

One can derive a useful representation of the transfer matrix $\mathbf{M}_{1,2} \equiv \mathbf{M}(s_1, s_2)$ between two points of a transfer line in terms of the generalized Twiss functions. Using the definitions of eigenvector and matrix $\mathbf{V}$ (see Eqs. (2.16) and (2.41)), one can derive the following identity:

$$\mathbf{V}_2\,\mathbf{S} = \mathbf{M}_{12}\,\mathbf{V}_1. \tag{2.58}$$

Here $\mathbf{V}_1$ and $\mathbf{V}_2$ are the $\mathbf{V}$-matrices given by Eq. (2.52) for the initial and final points. The matrix $\mathbf{S}$ is

$$\mathbf{S} = \begin{bmatrix} \cos\Delta\mu_1 & \sin\Delta\mu_1 & 0 & 0 \\ -\sin\Delta\mu_1 & \cos\Delta\mu_1 & 0 & 0 \\ 0 & 0 & \cos\Delta\mu_2 & \sin\Delta\mu_2 \\ 0 & 0 & -\sin\Delta\mu_2 & \cos\Delta\mu_2 \end{bmatrix}, \tag{2.59}$$

where $\Delta\mu_{1,2}$ are the betatron phase advances between points 1 and 2 for the first and second modes. Multiplying both sides of Eq. (2.59) by the inverse matrix, ${\mathbf{V}_1}^{-1} = -\mathbf{U}{\mathbf{V}_1}^{\mathrm{T}}\mathbf{U}$, as given by Eq. (2.9), allows one to express the transfer matrix, $\mathbf{M}_{12}$, in the form

$$\mathbf{M}_{12} = -\mathbf{V}_2\mathbf{S}\mathbf{U}{\mathbf{V}_1}^{\mathrm{T}}\mathbf{U}. \tag{2.60}$$

In the case of the one-turn transfer matrix, the matrices $\mathbf{V}_1$ and $\mathbf{V}_2$ are equal and Eq. (2.60) simplifies. That results in the following expressions for the matrix elements of diagonal 2×2 sub-matrices:

$$\begin{aligned} M_{11} &= (1-u)\cos\mu_1 + \alpha_{1x}\sin\mu_1 + u\cos\mu_2 + \alpha_{2x}\sin\mu_2, \\ M_{12} &= \beta_{1x}\sin\mu_1 + \beta_{2x}\sin\mu_2, \\ M_{21} &= -\frac{(1-u)^2+\alpha_{1x}^2}{\beta_{1x}}\sin\mu_1 - \frac{u^2+\alpha_{2x}^2}{\beta_{2x}}\sin\mu_2, \\ M_{22} &= (1-u)\cos\mu_1 + u\cos\mu_2 - \alpha_{1x}\sin\mu_1 - \alpha_{2x}\sin\mu_2, \end{aligned}$$

[3] The Tevatron lattice is based on the detailed optics measurement and takes into account large coupling terms coming mainly from the skew-quadrupole components of the superconducting dipoles. If the coupling corrections are adjusted to minimize the tune split, the value of coupling parameter u varies along the lattice in the range of about [−0.002, 0.04].

$$
\begin{aligned}
M_{33} &= u\cos\mu_1 + (1-u)\cos\mu_2 + \alpha_{2y}\sin\mu_2 + \alpha_{1y}\sin\mu_1, \\
M_{34} &= \beta_{1y}\sin\mu_1 + \beta_{2y}\sin\mu_2, \\
M_{43} &= -\frac{u^2+\alpha_{1y}^2}{\beta_{1y}}\sin\mu_1 - \frac{(1-u)^2+\alpha_{2y}^2}{\beta_{2y}}\sin\mu_2, \\
M_{44} &= u\cos\mu_1 + (1-u)\cos\mu_2 - \alpha_{1y}\sin\mu_1 - \alpha_{2y}\sin\mu_2,
\end{aligned}
\tag{2.61}
$$

where μ_1 and μ_2 are the betatron tunes of two betatron modes. The elements for off-diagonal sub-matrices can be found in [3].

We also present here the elements of matrix $\boldsymbol{\Sigma}$ used in other chapters of this book (see Eq. (2.25)):

$$
\begin{aligned}
&\Sigma_{11} \equiv \langle x^2\rangle = \varepsilon_1\beta_{1x} + \varepsilon_2\beta_{2x}, \quad \Sigma_{33} \equiv \langle y^2\rangle = \varepsilon_1\beta_{1y} + \varepsilon_2\beta_{2y}, \\
&\Sigma_{12} \equiv \langle xp_x\rangle = \Sigma_{21} = -\varepsilon_1\alpha_{1x} - \varepsilon_2\alpha_{2x}, \quad \Sigma_{34} \equiv \langle yp_y\rangle = \Sigma_{43} = -\varepsilon_1\alpha_{1y} - \varepsilon_2\alpha_{2y}, \\
&\Sigma_{13} \equiv \langle xy\rangle = \Sigma_{31} = \varepsilon_1\sqrt{\beta_{1x}\beta_{1y}}\cos\nu_1 + \varepsilon_2\sqrt{\beta_{2x}\beta_{2y}}\cos\nu_2, \\
&\Sigma_{22} \equiv \langle {p_x}^2\rangle = \varepsilon_1\frac{(1-u)^2+{\alpha_{1x}}^2}{\beta_{1x}} + \varepsilon_2\frac{u^2+{\alpha_{2x}}^2}{\beta_{2x}}, \\
&\Sigma_{44} \equiv \langle {p_y}^2\rangle = \varepsilon_1\frac{u^2+{\alpha_{1y}}^2}{\beta_{1y}} + \varepsilon_2\frac{(1-u)^2+{\alpha_{2y}}^2}{\beta_{2y}}, \\
&\Sigma_{24} \equiv \langle p_xp_y\rangle = \Sigma_{42} = \varepsilon_1\frac{\big(\alpha_{1y}(1-u) - \alpha_{1x}u\big)\sin\nu_1 + \big(u(1-u) + \alpha_{1x}\alpha_{1y}\big)\cos\nu_1}{\sqrt{\beta_{1x}\beta_{1y}}} \\
&\qquad\qquad + \varepsilon_2\frac{\big(\alpha_{2x}(1-u) - \alpha_{2y}u\big)\sin\nu_2 + \big(u(1-u) + \alpha_{2x}\alpha_{2y}\big)\cos\nu_2}{\sqrt{\beta_{2x}\beta_{2y}}}.
\end{aligned}
\tag{2.62}
$$

For other elements of matrix $\boldsymbol{\Sigma}$ and the expression of matrix $\boldsymbol{\Xi}$, we refer reader to [3].

2.1.8 Edwards–Teng Parameterization

The material presented in Sects. 2.1.5, 2.1.6, and 2.1.7 is based on the extension of the Mais–Ripken parameterization presented in [3]. However, the consideration of coupled motion would be incomplete without a discussion of the Edwards–Teng parameterization [6], which was proposed earlier and is presently one of the most popular parameterizations for description of coupled optics. It is based on a canonical transform $\mathbf{R}$ which reduces a 4×4 transfer matrix

$$\mathbf{M} = \begin{bmatrix} \mathbf{P} & \mathbf{p} \\ \mathbf{q} & \mathbf{Q} \end{bmatrix} \tag{2.63}$$

to its normal mode form

$$\widetilde{\mathbf{M}} = \mathbf{R}\mathbf{M}\mathbf{R}^{-1}, \tag{2.64}$$

where

$$\widetilde{\mathbf{M}} = \begin{bmatrix} \mathbf{A} & \mathbf{0} \\ \mathbf{0} & \mathbf{B} \end{bmatrix} \tag{2.65}$$

and **P**, **p**, **Q**, **q**, **A,** and **B** are 2×2 matrices. Edwards and Teng suggested parameterizing a symplectic matrix **R** as follows:

$$\mathbf{R} = \begin{bmatrix} \mathbf{E}\cos\phi & -\mathbf{D}^{-1}\sin\phi \\ \mathbf{D}\sin\phi & \mathbf{E}\cos\phi \end{bmatrix}, \tag{2.66}$$

where **E** is the unit 2×2 matrix and **D** is a 2×2 symplectic matrix,

$$\mathbf{D} = \begin{bmatrix} a & b \\ c & d \end{bmatrix}. \tag{2.67}$$

Thus, matrix **R** is parameterized by four parameters: a, b, c, and ϕ. Matrix $\widetilde{\mathbf{M}}$ describes the particle motion in new coordinates and can be parameterized by six Twiss parameters: $\beta_1, \alpha_1, \mu_1, \beta_2, \alpha_2$, and μ_2 which are called the Twiss parameters of the decoupled motion. Edwards and Teng expressed them through the transfer matrix elements. Here we present their connection to the extended Mais–Ripken parameterization considered above:

$$\begin{aligned} &\sin\phi = \pm\sqrt{u}, \\ &\beta_1 = \frac{\beta_{1x}}{1-u}, \quad \alpha_1 = \frac{\alpha_{1x}}{1-u}, \quad \beta_2 = \frac{\beta_{2y}}{1-u}, \quad \alpha_2 = \frac{\alpha_{2y}}{1-u}, \end{aligned} \tag{2.68}$$

$$\mathbf{R} = \frac{\pm 1}{\sqrt{1-u}} \begin{bmatrix} 1 & 0 & -d_t & b_t \\ 0 & 1 & c_t & -a_t \\ a_t & b_t & 1 & 0 \\ c_t & d_t & 0 & 1 \end{bmatrix}, \quad \begin{aligned} a_t &= \sqrt{\beta_{2y}/\beta_{2x}}\,(\alpha_{2x}\sin\nu_2 + u\cos\nu_2), \\ b_t &= \sqrt{\beta_{1x}\beta_{1y}}\,\sin\nu_1, \\ d_t &= -\sqrt{\beta_{1x}/\beta_{1y}}\,\big(u\cos\nu_1 + \alpha_{1y}\sin\nu_1\big), \\ c_t &= (a_t d_t + u - 1)/b_t. \end{aligned} \tag{2.69}$$

Details of calculations can be found in [3]. Although, the top Eq. (2.68) yields four different solutions for angle ϕ, there are unique solutions for the beta- and alpha-functions of the decoupled motion and matrix **R**. Note that the choice of sign

for matrix $\mathbf{R}$ in Eq. (2.69) is determined by the requirement that $\sqrt{\beta_{1,2}}$ are positive. However, a problem appears if the value of u is negative somewhere in the lattice. That results in ϕ being purely imaginary. The solution considered in [6] suggests a replacement of $\sin(\phi)$ and $\cos(\phi)$ by $\sinh(\phi)$ and $\cosh(\phi)$ with an appropriate sign changes in the symplectic transform of Eq. (2.66). It formally addresses the issue but still requires a redefinition of Eq. (2.66) symplectic transforms every time u changes its sign.

Edwards and Teng determined the phase advance of the betatron motion using a standard recipe for the uncoupled motion:

$$\widetilde{\mathbf{v}}_i(s)\mathrm{e}^{-i\mu_i(s)} = \widetilde{\mathbf{M}}(0,s)\widetilde{\mathbf{v}}_i(0), \tag{2.70}$$

where $\widetilde{\mathbf{v}}_i(s)$ are the eigenvectors of decoupled motion. It is important to note that the betatron phase advances of both parameterizations are equal; i.e., the betatron phase advance for the Edwards–Teng representation is directly related to particle oscillations in the x or y plane, depending on which plane a particular eigenvector is referenced to.

As will be shown in the next section, the value of u is changing fast if a system approaches the coupling resonance. Consequently, the beta-functions of extended Mais–Ripken parameterization also change fast although the sums $\beta_{1x}+\beta_{2x}$ and $\beta_{1y}+\beta_{2y}$ stay approximately constant. In contrast, the Edwards–Teng beta-functions are insensitive to the coupling resonance, while ϕ and matrix $\mathbf{R}$ are sensitive.

2.1.9 Betatron Tunes

Substituting the ring transfer matrix expressed in the block form of Eq. (2.63) into the symplecticity conditions of Eqs. (2.8) and (2.10) and performing matrix multiplication, one obtains

$$\begin{aligned}
\begin{bmatrix} \mathbf{P}^{\mathrm{T}}\mathbf{U}_2\mathbf{P}+\mathbf{q}^{\mathrm{T}}\mathbf{U}_2\mathbf{q} & \mathbf{P}^{\mathrm{T}}\mathbf{U}_2\mathbf{p}+\mathbf{q}^{\mathrm{T}}\mathbf{U}_2\mathbf{Q} \\ \mathbf{p}^{\mathrm{T}}\mathbf{U}_2\mathbf{P}+\mathbf{Q}^{\mathrm{T}}\mathbf{U}_2\mathbf{q} & \mathbf{p}^{\mathrm{T}}\mathbf{U}_2\mathbf{p}+\mathbf{Q}^{\mathrm{T}}\mathbf{U}_2\mathbf{Q} \end{bmatrix} &= \begin{bmatrix} \mathbf{U}_2 & 0 \\ 0 & \mathbf{U}_2 \end{bmatrix}, \\
\begin{bmatrix} \mathbf{P}\mathbf{U}_2\mathbf{P}^{\mathrm{T}}+\mathbf{p}\mathbf{U}_2\mathbf{p}^{\mathrm{T}} & \mathbf{P}\mathbf{U}_2\mathbf{q}^{\mathrm{T}}+\mathbf{p}\mathbf{U}_2\mathbf{Q}^{\mathrm{T}} \\ \mathbf{q}\mathbf{U}_2\mathbf{P}^{\mathrm{T}}+\mathbf{Q}\mathbf{U}_2\mathbf{p}^{\mathrm{T}} & \mathbf{q}\mathbf{U}_2\mathbf{q}^{\mathrm{T}}+\mathbf{Q}\mathbf{U}_2\mathbf{Q}^{\mathrm{T}} \end{bmatrix} &= \begin{bmatrix} \mathbf{U}_2 & 0 \\ 0 & \mathbf{U}_2 \end{bmatrix},
\end{aligned} \tag{2.71}$$

where $\mathbf{U}_2$ is the two-dimensional unit symplectic matrix.

Expanding the diagonal sub-matrices, one obtains four scalar equations:

$$\begin{aligned}
\det(\mathbf{P})+\det(\mathbf{q}) &= 1, \quad \det(\mathbf{p})+\det(\mathbf{Q}) = 1, \\
\det(\mathbf{P})+\det(\mathbf{p}) &= 1, \quad \det(\mathbf{q})+\det(\mathbf{Q}) = 1.
\end{aligned} \tag{2.72}$$

The solution of above equations yields that the determinants for two diagonal and two off-diagonal matrices are equal:

$$\kappa = \det(\mathbf{p}) = \det(\mathbf{q}), \quad 1 - \kappa = \det(\mathbf{P}) = \det(\mathbf{Q}), \tag{2.73}$$

where parameter κ characterizes the coupling strength. The off-diagonal sub-matrices in each matrix equation of Eq. (2.71) are related by matrix transpose, and the matrix equations are linearly dependent leaving only four independent scalar equations. That bounds up matrices $\mathbf{p}$ and $\mathbf{q}$:

$$\mathbf{p} = \mathbf{U}_2\left(\mathbf{P}^{\mathrm{T}}\right)^{-1}\mathbf{q}^{\mathrm{T}}\mathbf{U}_2\mathbf{Q} = \frac{1}{1-\kappa}\mathbf{P}\mathbf{U}_2\mathbf{q}^{\mathrm{T}}\mathbf{U}_2\mathbf{Q}, \tag{2.74}$$

where we took into account that $\mathbf{P}^{-1} = -\mathbf{U}_2\mathbf{P}^{\mathrm{T}}\mathbf{U}_2/(1-\kappa)$.

To separate coupling effects from effects of uncoupled betatron motion, let us consider the betatron motion in the normalized coordinates, so that in the new coordinates the ring transfer matrix would be presented in the following form:

$$\begin{aligned} \mathbf{M}_c &= \begin{bmatrix} \mathbf{P}_c & \mathbf{p}_c \\ \mathbf{q}_c & \mathbf{Q}_c \end{bmatrix}, \quad \mathbf{P}_c = \sqrt{1-\kappa}\begin{bmatrix} \cos\mu_x & \sin\mu_x \\ -\sin\mu_x & \cos\mu_x \end{bmatrix}, \\ \mathbf{Q}_c &= \sqrt{1-\kappa}\begin{bmatrix} \cos\mu_y & \sin\mu_y \\ -\sin\mu_y & \cos\mu_y \end{bmatrix}, \end{aligned} \tag{2.75}$$

where we explicitly took into account that $\det(\mathbf{P}_c) = \det(\mathbf{Q}_c)$. Here and below we denote by index c the vectors and matrices in the normalized coordinate frame. A symplectic matrix $\mathbf{R}_c$ performs transformation from the old to the new coordinates, $\mathbf{x}_c = \mathbf{R}_c\mathbf{x}$, and can be chosen in the following form:

$$\begin{aligned} \mathbf{R}_c &= \begin{bmatrix} \mathbf{R}_{cx} & 0 \\ 0 & \mathbf{R}_{cy} \end{bmatrix}, \quad \mathbf{R}_{cx} = \begin{bmatrix} 1/\sqrt{\beta_{xc}} & 0 \\ \alpha_{xc}/\sqrt{\beta_{xc}} & \sqrt{\beta_{xc}} \end{bmatrix}, \\ \mathbf{R}_{cy} &= \begin{bmatrix} 1/\sqrt{\beta_{yc}} & 0 \\ \alpha_{yc}/\sqrt{\beta_{yc}} & \sqrt{\beta_{yc}} \end{bmatrix}. \end{aligned} \tag{2.76}$$

Then, the ring transfer matrix in the normalized coordinates is $\mathbf{M}_c = \mathbf{R}_c\mathbf{M}\mathbf{R}_c^{-1}$. Performing matrix multiplication and requiring the resulting matrix to be in the form of Eq. (2.75), one obtains the parameters of matrix $\mathbf{R}_c$:

$$\begin{aligned} \beta_{xc} &= \sqrt{\frac{-4M_{12}{}^2}{4M_{12}M_{21} + (M_{11} - M_{22})^2}}, \quad \alpha_{xc} = \beta_{xc}\frac{M_{11} - M_{22}}{2M_{12}}, \\ \beta_{yc} &= \sqrt{\frac{-4M_{34}{}^2}{4M_{34}M_{43} + (M_{33} - M_{44})^2}}, \quad \alpha_{yc} = \beta_{yc}\frac{M_{33} - M_{44}}{2M_{34}}. \end{aligned} \tag{2.77}$$

The symplectic transform does not change the trace of the diagonal sub-matrices. That yields

$$\begin{aligned}\cos\mu_x &= \frac{\mathrm{tr}(\mathbf{P}_c)}{2(1-\kappa)} = \frac{\mathrm{tr}(\mathbf{P})}{2(1-\kappa)} = \frac{M_{11}+M_{22}}{2(1-\kappa)},\\ \cos\mu_y &= \frac{\mathrm{tr}(\mathbf{Q}_c)}{2(1-\kappa)} = \frac{\mathrm{tr}(\mathbf{Q})}{2(1-\kappa)} = \frac{M_{33}+M_{44}}{2(1-\kappa)}.\end{aligned} \tag{2.78}$$

The off-diagonal sub-matrices of matrix $\mathbf{M}_c$ are

$$\mathbf{q}_c \equiv \begin{bmatrix} a_c & b_c \\ c_c & d_c \end{bmatrix} = \mathbf{R}_{cx}\mathbf{q}{\mathbf{R}_{cy}}^{-1}, \quad \mathbf{p}_c \equiv \begin{bmatrix} \hat{a}_c & \hat{b}_c \\ \hat{c}_c & \hat{d}_c \end{bmatrix} = \mathbf{R}_{cx}\mathbf{p}{\mathbf{R}_{cy}}^{-1}. \tag{2.79}$$

Note that Eq. (2.74) uniquely couples a_c, b_c, c_c, and d_c with $\hat{a}_c, \hat{b}_c, \hat{c}_c$, and $\hat{d}_c$. That leaves only four independent parameters for coupling characterization out of eight parameters of off-diagonal sub-matrices. There is another useful property of matrices $\mathbf{P}_c$, $\mathbf{Q}_c$, $\mathbf{p}_c$, and $\mathbf{q}_c$:

$$\mathrm{tr}\left({\mathbf{P}_c}^{\mathrm{T}}\mathbf{P}_c\right) = \mathrm{tr}\left({\mathbf{Q}_c}^{\mathrm{T}}\mathbf{Q}_c\right), \quad \mathrm{tr}\left({\mathbf{p}_c}^{\mathrm{T}}\mathbf{p}_c\right) = \mathrm{tr}\left({\mathbf{q}_c}^{\mathrm{T}}\mathbf{q}_c\right). \tag{2.80}$$

The first equation follows from the definitions of $\mathbf{P}_c$ and $\mathbf{Q}_c$. The following string of conversions proves the second equation:

$$\begin{aligned}\mathrm{tr}\left({\mathbf{p}_c}^{\mathrm{T}}\mathbf{p}_c\right) &= \mathrm{tr}\left(\left(\mathbf{U}_2\left({\mathbf{P}_c}^{\mathrm{T}}\right)^{-1}{\mathbf{q}_c}^{\mathrm{T}}\mathbf{U}_2\mathbf{Q}_c\right)^{\mathrm{T}}\mathbf{U}_2\left({\mathbf{P}_c}^{\mathrm{T}}\right)^{-1}{\mathbf{q}_c}^{\mathrm{T}}\mathbf{U}_2\mathbf{Q}_c\right)\\ &= \mathrm{tr}\left({\mathbf{Q}_c}^{\mathrm{T}}\mathbf{U}_2\mathbf{q}_c{\mathbf{P}_c}^{-1}\mathbf{U}_2\mathbf{U}_2\left({\mathbf{P}_c}^{\mathrm{T}}\right)^{-1}{\mathbf{q}_c}^{\mathrm{T}}\mathbf{U}_2\mathbf{Q}_c\right)\\ &= -\mathrm{tr}\left({\mathbf{Q}_c}^{\mathrm{T}}\mathbf{U}_2\mathbf{q}_c{\mathbf{P}_c}^{-1}\left({\mathbf{P}_c}^{\mathrm{T}}\right)^{-1}{\mathbf{q}_c}^{\mathrm{T}}\mathbf{U}_2\mathbf{Q}_c\right)\\ &= \frac{-1}{1-\kappa}\mathrm{tr}\left({\mathbf{Q}_c}^{\mathrm{T}}\mathbf{U}_2\mathbf{q}_c{\mathbf{q}_c}^{\mathrm{T}}\mathbf{U}_2\mathbf{Q}_c\right) = -\mathrm{tr}\left(\mathbf{U}_2\mathbf{q}_c{\mathbf{q}_c}^{\mathrm{T}}\mathbf{U}_2\right) = \mathrm{tr}\left(\mathbf{q}_c{\mathbf{q}_c}^{\mathrm{T}}\right).\end{aligned}$$

Here we used that ${\mathbf{P}_c}^{-1} = {\mathbf{P}_c}^{\mathrm{T}}/(1-\kappa)$, ${\mathbf{Q}_c}^{-1} = {\mathbf{Q}_c}^{\mathrm{T}}/(1-\kappa)$, $\mathbf{U}_2\mathbf{U}_2 = -\mathbf{I}$, and $\mathrm{tr}(\mathbf{AB}) = \mathrm{tr}(\mathbf{BA})$.

To find the betatron tunes, we follow the standard recipe for finding roots of dispersion equation: $\det(\mathbf{M}_c - \lambda\mathbf{I}) = 0$. Computing the determinant and performing further simplifications, we obtain

$$\begin{aligned}&\lambda^4 - 2\sqrt{1-\kappa}\left(\cos\mu_x + \cos\mu_y\right)\left(\lambda^3+\lambda\right)\\ &\quad + \left(2(1-\kappa)\left(1+\cos\mu_x\cos\mu_y\right) - \mathrm{tr}(\mathbf{p}_c\mathbf{q}_c)\right)\lambda^2 + 1\\ &\quad = 0.\end{aligned} \tag{2.81}$$

In the case of stable motion, the solution of Eq. (2.81) consists of two complex conjugated pairs. The corresponding fourth-order polynomial can be presented in the following form:

$$\prod_{i=1}^{4}(\lambda-\lambda_i)=\left(\lambda^2-2\lambda\cos\mu_1+1\right)\left(\lambda^2-2\lambda\cos\mu_2+1\right)$$
$$=\lambda^4-2\left(\lambda^3+\lambda\right)(\cos\mu_1+\cos\mu_2)+2(1+2\cos\mu_1\cos\mu_2)\lambda^2+1=0. \tag{2.82}$$

Comparing Eqs. (2.81) and (2.82), we obtain the following system of equations:

$$\begin{aligned}&\cos\mu_1+\cos\mu_2=\sqrt{1-\kappa}\left(\cos\mu_x+\cos\mu_y\right),\\&1+\cos\mu_1\cos\mu_2=(1-\kappa)\left(1+\cos\mu_x\cos\mu_y\right)-\mathrm{tr}(\mathbf{p}_c\mathbf{q}_c)/2.\end{aligned} \tag{2.83}$$

The solution is

$$\cos\mu_{1,2}=\sqrt{1-\kappa}\frac{\cos\mu_x+\cos\mu_y}{2}$$
$$\pm\sqrt{(1-\kappa)\left(\frac{\cos\mu_x-\cos\mu_y}{2}\right)^2+\frac{1}{2}\left(\kappa+\frac{1}{2}\mathrm{tr}(\mathbf{p}_c\mathbf{q}_c)\right)}. \tag{2.84}$$

The same as sub-matrices **p** and **q,** the sub-matrices $\mathbf{p}_c$ and $\mathbf{q}_c$ are related by Eq. (2.74). That allows one to express $\mathrm{tr}(\mathbf{p}_c\mathbf{q}_c)$ through matrix $\mathbf{q}_c$. Performing matrix multiplication, one obtains

$$\mathrm{tr}(\mathbf{p}_c\mathbf{q}_c)=\frac{1}{1-\kappa}\mathrm{tr}\left(\mathbf{P}_c\mathbf{U}_2\mathbf{q}_c{}^{\mathrm{T}}\mathbf{U}_2\mathbf{Q}_c\mathbf{q}_c\right)=\sin\mu_x\sin\mu_y\mathrm{tr}\left(\mathbf{q}_c{}^{\mathrm{T}}\mathbf{q}_c\right)-2\cos\mu_x\cos\mu_y\det(\mathbf{q}_c)$$
$$=\sin\mu_x\sin\mu_y\left(a_c{}^2+b_c{}^2+c_c{}^2+d_c{}^2\right)-2\cos\mu_x\cos\mu_y(a_cd_c-b_cc_c). \tag{2.85}$$

To express the tunes directly through the transfer matrix elements, we take into account that the coefficients in Eq. (2.81) do not change when we perform a transform to the normalized coordinates. In particular it means that coefficients in front of λ and λ^3 are equal. It simplifies the calculations. As a result, we obtain the dispersion equation:

$$\lambda^4-\mathrm{tr}(\mathbf{M})\left(\lambda^3+\lambda\right)+\Lambda\lambda^2+1=0, \tag{2.86}$$

where

$$\begin{aligned}\Lambda=&(M_{11}M_{22}-M_{12}M_{21})+(M_{33}M_{44}-M_{34}M_{43})+(M_{11}M_{33}-M_{13}M_{31})\\&+(M_{11}M_{44}-M_{14}M_{41})+(M_{33}M_{22}-M_{23}M_{32})+(M_{22}M_{44}-M_{24}M_{42}).\end{aligned} \tag{2.87}$$

Then, the solution is [6]

$$\cos\mu_{1,2} = \frac{1}{4}\left(\mathrm{tr}(\mathbf{M}) \pm \sqrt{(\mathrm{tr}(\mathbf{M}))^2 + 8 - 4\Lambda}\right). \tag{2.88}$$

2.1.10 Coupling Strength, Tune Split, and Width of Resonance Stop Band

There is no single parameter to completely characterize coupling. However, the parameter u (see Eq. (2.51)) is one of the most informative. It characterizes the relative contributions of x and y parts to the eigenvector normalization of Eq. (2.14), so that they are proportional to u or $1-u$. In the absence of coupling, the parameter u is equal to 0 (or 1 if x and y vectors are swapped). Note that, in the general case, the equality $u=0$ does not imply an absence of coupling. As one can see from Eqs. (2.45) and (2.49), the condition $u=0$ requires ${A_x}^2+{\kappa_x}^2={A_y}^2+{\kappa_y}^2$ and yields $e^{i\nu_+} = (A_x+i\kappa_x)/(A_y-i\kappa_y)$ and $e^{i\nu_-} = (A_x+i\kappa_x)/(A_y+i\kappa_y)$. These equations do not require auxiliary beta-functions β_{1y} and β_{2x} to be equal to zero, and, consequently, the condition $u=0$ does not automatically mean an absence of coupling. Although strictly speaking u cannot be considered as a unique coupling parameter, it reflects the strength of coupling and is a good value to characterize it in practice. In particular $u=½$ corresponds to 100 % coupling when the motion for both eigenvectors is equally distributed in both planes. It is also useful to note that u does not change in the part of a beamline without coupling terms. Actually, in the absence of coupling, the x and y parts of the eigenvector, $\mathbf{v}_x$ and $\mathbf{v}_y$, are independent and their normalization, $\mathbf{v}_{x,y}{}^{+}\mathbf{U}_2\mathbf{v}_{x,y}=\{u,\ 1-u\}$, does not change because the determinants of the corresponding 2×2 transfer matrices are equal to 1. Here $\mathbf{U}_2$ is the 2D unit symplectic matrix.

To express the value of u through the betatron tunes, we add up the matrix elements M_{11} and M_{22} of Eq. (2.61). That yields $M_{11}+M_{22}=2(1-u)\cos\mu_1+2u\cos\mu_2$. Taking into account that it is also justified for $M_{c_{11}}+M_{c_{22}}$ and by definition $M_{c_{11}}+M_{c_{22}}=2\sqrt{1-\kappa}\cos\mu_x$, we obtain

$$\sqrt{1-\kappa}\cos\mu_x = (1-u)\cos\mu_1 + u\cos\mu_2.$$

That results in

$$u = \frac{\sqrt{1-\kappa}\cos\mu_x - \cos\mu_1}{\cos\mu_2 - \cos\mu_1}. \tag{2.89}$$

Let coupling be small,[4] $\mathrm{tr}(\mathbf{q}_c{}^{\mathrm{T}}\mathbf{q}_c)\ll 1$, and tunes be located in the vicinity of difference coupling resonance. Then, the fractional parts of the tunes, $\hat{\mu}_x, \hat{\mu}_y, \hat{\mu}_1$,

[4] The condition $\mathrm{tr}(\mathbf{q}_c{}^{\mathrm{T}}\mathbf{q}_c)\ll 1$ also results in that $|\kappa|\ll 1$. Actually, expressing both equations through the matrix elements, one obtains $\mathrm{tr}(\mathbf{q}_c{}^{\mathrm{T}}\mathbf{q}_c)=a^2+b^2+c^2+d^2$ and $\kappa\equiv\det(\mathbf{q}_c)=ad-bc$. Obviously, $|ad-bc|<a^2+b^2+c^2+d^2$.

and $\hat{\mu}_2$, are close to each other, and we introduce the following definitions: $\Delta\mu = \hat{\mu}_x - \hat{\mu}_y \ll 1$, $\hat{\mu}_1 = \hat{\mu}_x + \Delta\mu_1$, and $\hat{\mu}_2 = \hat{\mu}_x + \Delta\mu_2$. Consequently, we expand Eq. (2.84) into Taylor series:

$$\cos\mu_x - \Delta\mu_{1,2}\sin\mu_x \approx \left(1 - \frac{\kappa}{2}\right)\frac{2\cos\mu_x - \Delta\mu\sin\mu_x}{2} \pm \sqrt{\left(\frac{\Delta\mu\sin\mu_x}{2}\right)^2 + \frac{1}{2}\left(\kappa + \frac{1}{2}\mathrm{tr}(\mathbf{p}_c\mathbf{q}_c)\right)}. \tag{2.90}$$

Simplifying the above equation with the help of Eq. (2.85), leaving only the leading order terms and returning to the tunes from their differentials, we obtain

$$\hat{\mu}_{1,2} \approx \frac{1}{2}\left((\hat{\mu}_x + \hat{\mu}_y) \pm \sqrt{(\hat{\mu}_x - \hat{\mu}_y)^2 + \delta\mu_d{}^2}\right), \quad |\hat{\mu}_x - \hat{\mu}_y|, \delta\mu_d \ll 1, \tag{2.91}$$

where

$$\delta\mu_d = \sqrt{(a_c + d_c)^2 + (b_c - c_c)^2} = \sqrt{(\hat{a}_c + \hat{d}_c)^2 + (\hat{b}_c - \hat{c}_c)^2} \tag{2.92}$$

represents the minimum tune split. Substitution of Eq. (2.91) to Eq. (2.89) results in the coupling strength dependence on the tunes in the vicinity of difference coupling resonance:

$$u \approx \frac{1}{2}\left(1 - \frac{\hat{\mu}_x - \hat{\mu}_y}{\sqrt{(\hat{\mu}_x - \hat{\mu}_y)^2 + \delta\mu_d{}^2}}\right), \quad |\hat{\mu}_x - \hat{\mu}_y|, \quad \delta\mu_d \ll 1. \tag{2.93}$$

If $\hat{\mu}_x = \hat{\mu}_y$, the coupling parameter is equal to 1/2. That corresponds to 100 % coupled motion. In the case of $|\hat{\mu}_x - \hat{\mu}_y| \gg \delta\mu_d$, the coupling strength, u, is small (or close to one if the order of tunes is reversed.) That corresponds to a weakly coupled motion.

If the tunes are located in the vicinity of coupling sum resonance, then $\hat{\mu}_x + \hat{\mu}_y - 2\pi = \Delta\mu \ll 1$. Introducing the following definitions, $\hat{\mu}_1 = \hat{\mu}_x + \Delta\mu_1$ and $\hat{\mu}_2 = 2\pi - \hat{\mu}_x + \Delta\mu_2$, and expanding Eq. (2.84) into Taylor series, we obtain

$$\cos\mu_x - \Delta\mu_1\sin\mu_x \approx \left(1 - \frac{\kappa}{2}\right)\frac{2\cos\mu_x + \Delta\mu\sin\mu_x}{2} - \sqrt{\left(\frac{\Delta\mu\sin\mu_x}{2}\right)^2 + \frac{1}{2}\left(\kappa + \frac{1}{2}\mathrm{tr}(\mathbf{p}_c\mathbf{q}_c)\right)}. \tag{2.94}$$

Simplifying the above equation with the help of Eq. (2.85), leaving only leading order terms, repeating similar expansion for $\Delta\mu_2$, and returning to the tunes from their differentials, we obtain

$$\hat{\mu}_{1,2} \approx \frac{1}{2}\left(\pm\left(\hat{\mu}_x - \hat{\mu}_y\right) + 2\pi + \sqrt{\left(\hat{\mu}_x + \hat{\mu}_y - 2\pi\right)^2 - \delta\mu_s{}^2}\right), \quad \left|2\pi - \left(\hat{\mu}_x + \hat{\mu}_y\right)\right|, \delta\mu_s \ll 1, \tag{2.95}$$

where

$$\delta\mu_s = \sqrt{(a_c - d_c)^2 + (b_c + c_c)^2} = \sqrt{\left(\hat{a}_c - \hat{d}_c\right)^2 + \left(\hat{b}_c + \hat{c}_c\right)^2} \tag{2.96}$$

represents the total width of the resonance stop band. One can see that tunes μ_1 and μ_2 become imaginary if the tunes μ_x and μ_y are located inside the resonance stop band. Consequently, the particle motion becomes unstable.

2.1.11 Perturbation Theory for Coupled Motion

The symplecticity allows one to build an effective perturbation theory for the case of coupled motion. Let the unperturbed motion eigenvalues and eigenvectors be related by Eq. (2.11). Then, for the perturbed motion one can write

$$(\mathbf{I} + \mathbf{\Delta M})\mathbf{M}\widetilde{\mathbf{v}}_j = \left(\lambda_j + \Delta\lambda_j\right)\widetilde{\mathbf{v}}_j, \tag{2.97}$$

where the new transfer matrix, $(\mathbf{I} + \mathbf{\Delta M})\mathbf{M}$, is not necessarily a symplectic matrix. The eigenvectors of perturbed motion can be presented as a sum of the unperturbed ones,

$$\widetilde{\mathbf{v}}_j = \mathbf{v}_j + \sum_{i=1}^{4} \varepsilon_{ij}\mathbf{v}_i, \quad \varepsilon_{ij} << 1, \tag{2.98}$$

and without limitation of generality, one can consider that $\varepsilon_{ii} = 0$ for every i. Substituting Eq. (2.98) into Eq. (2.97), linearizing the resulting equation, and using Eq. (2.11), one obtains

$$\sum_{i=1}^{4} \left(\lambda_i - \lambda_j\right)\varepsilon_{ij}\mathbf{v}_i = \left(\Delta\lambda_j\mathbf{I} - \mathbf{\Delta M} \;\; \mathbf{M}\right)\mathbf{v}_j. \tag{2.99}$$

In the case of stable unperturbed motion, the eigenvalues and eigenvectors represent two complex conjugate pairs. Taking this into account, $[\mathbf{v}_1 \;\; \mathbf{v}_2 \;\; \mathbf{v}_3 \;\; \mathbf{v}_4] \rightarrow [\mathbf{v}_1 \;\; \mathbf{v}_1{}^* \;\; \mathbf{v}_2 \;\; \mathbf{v}_2{}^*]$, and introducing complex matrix $\mathbf{V}_p = [\mathbf{v}_1 \;\; \mathbf{v}_1{}^* \;\; \mathbf{v}_2 \;\; \mathbf{v}_2{}^*]$, one can rewrite Eq. (2.99) in the form of two matrix equations:

$$\begin{aligned}
\mathbf{V}_p \begin{bmatrix} 1 & 0 & 0 & 0 \\ 0 & \lambda_1 - {\lambda_1}^* & 0 & 0 \\ 0 & 0 & \lambda_1 - \lambda_2 & 0 \\ 0 & 0 & 0 & \lambda_1 - {\lambda_2}^* \end{bmatrix} \begin{bmatrix} \Delta\lambda_1 \\ \varepsilon_{21} \\ \varepsilon_{31} \\ \varepsilon_{41} \end{bmatrix} &= \mathbf{\Delta M M} \mathbf{v}_1, \\
\mathbf{V}_p \begin{bmatrix} \lambda_2 - \lambda_1 & 0 & 0 & 0 \\ 0 & \lambda_2 - {\lambda_1}^* & 0 & 0 \\ 0 & 0 & 1 & 0 \\ 0 & 0 & 0 & \lambda_2 - {\lambda_2}^* \end{bmatrix} \begin{bmatrix} \varepsilon_{12} \\ \varepsilon_{22} \\ \Delta\lambda_2 \\ \varepsilon_{42} \end{bmatrix} &= \mathbf{\Delta M M} \mathbf{v}_2.
\end{aligned} \tag{2.100}$$

Matrix $\mathbf{V}_p$ is built from symplectic vectors and its inverse is equal to

$$\mathbf{V}_p{}^{-1} = -\frac{1}{2i} \mathbf{U} \mathbf{V}_p{}^{\mathrm{T}} \mathbf{U}. \tag{2.101}$$

One can verify it by utilizing the eigenvector normalization of Eq. (2.14). Inversion of Eq. (2.100) with the help of Eq. (2.101) finally results in [7]

$$\begin{aligned}
\begin{bmatrix} \Delta\lambda_1 \\ \varepsilon_{21} \\ \varepsilon_{31} \\ \varepsilon_{41} \end{bmatrix} &= -\frac{\lambda_1}{2i} \begin{bmatrix} 1 & 0 & 0 & 0 \\ 0 & \lambda_1 - {\lambda_1}^* & 0 & 0 \\ 0 & 0 & \lambda_1 - \lambda_2 & 0 \\ 0 & 0 & 0 & \lambda_1 - {\lambda_2}^* \end{bmatrix}^{-1} \mathbf{U} \mathbf{V}_c{}^{\mathrm{T}} \mathbf{U} \mathbf{\Delta M} \mathbf{v}_1, \\
\begin{bmatrix} \varepsilon_{12} \\ \varepsilon_{22} \\ \Delta\lambda_2 \\ \varepsilon_{42} \end{bmatrix} &= -\frac{\lambda_2}{2i} \begin{bmatrix} \lambda_2 - \lambda_1 & 0 & 0 & 0 \\ 0 & \lambda_2 - {\lambda_1}^* & 0 & 0 \\ 0 & 0 & 1 & 0 \\ 0 & 0 & 0 & \lambda_2 - {\lambda_2}^* \end{bmatrix}^{-1} \mathbf{U} \mathbf{V}_c{}^{\mathrm{T}} \mathbf{U} \mathbf{\Delta M} \mathbf{v}_2.
\end{aligned} \tag{2.102}$$

Multiplication of Eqs. (2.102) by $[1 \quad 0 \quad 0 \quad 0]$ and $[0 \quad 0 \quad 1 \quad 0]$, correspondingly, results in corrections for the eigenvalues:

$$\begin{aligned}
\Delta\lambda_1 &= -\frac{\lambda_1}{2i} \quad \mathbf{v}_1{}^{+} \mathbf{U} \mathbf{\Delta M} \mathbf{v}_1, \\
\Delta\lambda_2 &= -\frac{\lambda_2}{2i} \quad \mathbf{v}_2{}^{+} \mathbf{U} \mathbf{\Delta M} \mathbf{v}_2.
\end{aligned} \tag{2.103}$$

Taking into account the relationship between the eigenvalue corrections and the tune shifts, $\Delta Q_n = i/(4\pi)\ (\Delta\lambda_n/\lambda_n)$, one obtains [8]

$$\begin{aligned}
\Delta Q_1 &= -\frac{1}{4\pi} \mathbf{v}_1{}^{+} \mathbf{U} \mathbf{\Delta M} \mathbf{v}_1, \\
\Delta Q_2 &= -\frac{1}{4\pi} \mathbf{v}_2{}^{+} \mathbf{U} \mathbf{\Delta M} \mathbf{v}_2.
\end{aligned} \tag{2.104}$$

To demonstrate an application of the above formalism, let us find the tune shifts due to a local focusing perturbation. In the general case the perturbation of the

Hamiltonian is proportional to $\Phi_x x^2 + 2\Phi_s xy + \Phi_y y^2$. That results in the transfer matrix of the perturbation:

$$\mathbf{\Delta M} = \begin{bmatrix} 0 & 0 & 0 & 0 \\ -\Phi_x & 0 & -\Phi_s & 0 \\ 0 & 0 & 0 & 0 \\ -\Phi_s & 0 & -\Phi_y & 0 \end{bmatrix}.$$

Substituting it to Eq. (2.104), one obtains [7]

$$\begin{aligned} \Delta Q_1 &= \frac{1}{4\pi}\left(\Phi_x \beta_{1x} + 2\Phi_s \sqrt{\beta_{1x}\beta_{1y}} \cos\nu_1 + \Phi_y \beta_{1y}\right), \\ \Delta Q_2 &= \frac{1}{4\pi}\left(\Phi_x \beta_{2x} + 2\Phi_s \sqrt{\beta_{2x}\beta_{2y}} \cos\nu_2 + \Phi_y \beta_{2y}\right). \end{aligned} \tag{2.105}$$

One can see that in the case of uncoupled motion, $\beta_{1y} = \beta_{2x} = 0$, the tune shifts coincide with the well-known expression for the tune shift of uncoupled motion. Note that for a quadrupole field $\Phi_x = -\Phi_y$.

2.1.12 Sum and Difference Coupling Resonances

An analysis of the coupled motion using a perturbation theory applied directly to the equations describing initially uncoupled motion is useful in many applications. Let us consider the two uncoupled modes x and y. For each of them the formalism described in Sects. 2.1.1–2.1.7 can be reduced from four dimensional to two dimensional, so that

$$\begin{aligned} \mathbf{x}(s) &\equiv \begin{pmatrix} x \\ x' \end{pmatrix} = \mathrm{Re}\left(A_x \mathbf{v}_1(s) \mathrm{e}^{-i\mu_x(s)}\right) = \tfrac{1}{2} A_x \mathbf{v}_1(s) \mathrm{e}^{-i\mu_x(s)} + \tfrac{1}{2} A_x^* \mathbf{v}_1^*(s) \mathrm{e}^{i\mu_x(s)}, \\ \mathbf{y}(s) &\equiv \begin{pmatrix} y \\ y' \end{pmatrix} = \mathrm{Re}\left(A_y \mathbf{v}_2(s) \mathrm{e}^{-i\mu_y(s)}\right) = \tfrac{1}{2} A_y \mathbf{v}_2(s) \mathrm{e}^{-i\mu_y(s)} + \tfrac{1}{2} A_y^* \mathbf{v}_2^*(s) \mathrm{e}^{i\mu_y(s)}. \end{aligned} \tag{2.106}$$

Here A_x and A_y are the complex amplitudes of horizontal and vertical motion (the same as described by amplitudes A_1, A_2 and phases ψ_1, ψ_2 in Eq. (2.15)) and the eigenvectors $\mathbf{v}_1$, $\mathbf{v}_2$ are two-dimensional vectors:

$$\mathbf{v}_1 = \begin{pmatrix} \sqrt{\beta_x(s)} \\ -\dfrac{i+\alpha_x(s)}{\sqrt{\beta_x(s)}} \end{pmatrix}, \quad \mathbf{v}_2 = \begin{pmatrix} \sqrt{\beta_y(s)} \\ -\dfrac{i+\alpha_y(s)}{\sqrt{\beta_y(s)}} \end{pmatrix}. \tag{2.107}$$

One can express the amplitudes A_x, A_y via $\mathbf{x}(s)$ and $\mathbf{y}(s)$, correspondingly. Indeed, multiplying Eq. (2.106) by $\mathrm{e}^{i\mu_x(s)}\mathbf{v}_1^+ U$ or $\mathrm{e}^{i\mu_y(s)}\mathbf{v}_2^+ U$ on the left and using the orthogonality conditions in Eq. (2.14), one obtains

$$A_x = \frac{1}{i} e^{i\mu_x(s)} \mathbf{v}_1^+ \mathbf{U}_2 \mathbf{x}, \quad A_y = \frac{1}{i} e^{i\mu_y(s)} \mathbf{v}_2^+ \mathbf{U}_2 \mathbf{y}. \tag{2.108}$$

Here $\mathbf{U}_2$ is a 2×2 unit symplectic matrix. Now let us look for the solution of Eq. (2.6) in the form of Eq. (2.106), but with A_x, A_y not being constant. Substituting Eq. (2.106) into Eq. (2.6) and considering N and R as small perturbations, we obtain the equations for A_x, A_y:

$$\begin{aligned} \frac{dA_x}{ds} &= \frac{\mathrm{e}^{i\mu_x(s)}}{2i}\sqrt{\beta_x(s)\beta_y(s)}\left[-\left(N-\frac{R'}{2}\right)\left(A_y \mathrm{e}^{-i\mu_y(s)} + A_y^* \mathrm{e}^{i\mu_y(s)}\right)\right. \\ &\left. - R\left(A_y \frac{\alpha_y(s)+i}{\beta_y(s)} \mathrm{e}^{-i\mu_y(s)} + A_y^* \frac{\alpha_y(s)-i}{\beta_y(s)} \mathrm{e}^{i\mu_y(s)}\right)\right], \\ \frac{dA_y}{ds} &= \frac{\mathrm{e}^{i\mu_y(s)}}{2i}\sqrt{\beta_x(s)\beta_y(s)}\left[-\left(N+\frac{R'}{2}\right)\left(A_x \mathrm{e}^{-i\mu_x(s)} + A_x^* \mathrm{e}^{i\mu_x(s)}\right)\right. \\ &\left. + R\left(A_x \frac{\alpha_x(s)+i}{\beta_x(s)} \mathrm{e}^{-i\mu_x(s)} + A_x^* \frac{\alpha_x(s)-i}{\beta_x(s)} \mathrm{e}^{i\mu_x(s)}\right)\right]. \end{aligned} \tag{2.109}$$

In the vicinity of sum and difference resonances, Eq. (2.109) can be solved by averaging.

Near the sum resonance $\nu_x+\nu_y = k_+ + \Delta$, the system Eq. (2.109) reduces to

$$\begin{aligned} \frac{dA_x}{ds} &= C_+ A_y^* \mathrm{e}^{2i\pi\,\Delta\cdot s/C}, \\ \frac{dA_y}{ds} &= C_+ A_x^* \mathrm{e}^{2i\pi\,\Delta\cdot s/C}, \end{aligned} \tag{2.110}$$

where the resonance strength C_+ is defined by

$$C_+ = \frac{i}{2}\int_0^C \frac{ds}{C}\sqrt{\beta_x\beta_y}\left(2N + R\left[\left(\frac{\alpha_x}{\beta_x} - \frac{\alpha_y}{\beta_y}\right) - i\left(\frac{1}{\beta_x} - \frac{1}{\beta_y}\right)\right]\right)\mathrm{e}^{i\left(\mu_x+\mu_y-2\pi\left(\nu_x+\nu_y\right)s/C+2\pi k_+ s/C\right)}. \tag{2.111}$$

Here integration is performed over the machine circumference C. For the difference resonance $\nu_x - \nu_y = k_- + \Delta$, the equations are

$$\begin{aligned} \frac{dA_x}{ds} &= C_- A_y \mathrm{e}^{i2\pi\Delta\cdot s/C}, \\ \frac{dA_y}{ds} &= -C_-^* A_x \mathrm{e}^{-i2\pi\Delta\cdot s/C}, \end{aligned} \tag{2.112}$$

and the resonance strength is

$$C_- = \frac{i}{2}\int_0^C \frac{ds}{C}\sqrt{\beta_x\beta_y}\left(2N + R\left[\left(\frac{\alpha_x}{\beta_x} - \frac{\alpha_y}{\beta_y}\right) - i\left(\frac{1}{\beta_x} + \frac{1}{\beta_y}\right)\right]\right)\mathrm{e}^{i\left(\mu_x-\mu_y-2\pi\left(\nu_x-\nu_y\right)s/C+2\pi k_- s/C\right)}. \tag{2.113}$$

Integration of Eqs. (2.112) over one revolution binds up two complex resonance strengths, C_+ and C_-, to the elements of the off-diagonal sub-matrices $\mathbf{q}_c$ and $\mathbf{p}_c$ of Eq. (2.79).

2.1.13 *Emittance Growth at Beam Transfers Due to Optics Mismatch and* X–Y *Coupling*

As an application of the above-developed formalism, we consider here the emittance growth related to an optics mismatch at beam transfer from one ring to another. Let the incoming beam distribution function be Gaussian and be described by bilinear form Ξ (see Eq. (2.34)). The corresponding eigenvectors and $\mathbf{V}$-matrix we denote as $\mathbf{v}_1$, $\mathbf{v}_2$ and $\mathbf{V}$ (see Eqs. (2.16) and (2.32)). The eigenvectors and $\mathbf{V}$-matrix of the circulating beam we denote as $\mathbf{v}'_1, \mathbf{v}'_2$ and $\mathbf{V}'$. Rewriting Eq. (2.41), we express the coordinates of each particle at the injection point through their new actions (single-particle rms emittances) and new eigenvectors:

$$\mathbf{x} = \frac{1}{2}\left(\sqrt{2I'_1}\left(\mathbf{v}'_1\mathrm{e}^{i\psi_1} + \mathbf{v}'_1{*}\mathrm{e}^{-i\psi_1}\right) + \sqrt{2I'_2}\left(\mathbf{v}'_2\mathrm{e}^{i\psi_2} + \mathbf{v}'_2{*}\mathrm{e}^{-i\psi_2}\right)\right). \tag{2.114}$$

Multiplying each side of the above equation by $\mathbf{v}'^{+}_1\mathbf{U}$ or $\mathbf{v}'^{+}_2\mathbf{U}$ and using the orthogonality conditions of Eq. (2.14), we obtain

$$I'_k(\mathbf{x}) = \frac{1}{2}\left|\mathbf{v}_k{}^{+}\mathbf{U}\mathbf{x}\right|^2, \quad k = 1, 2. \tag{2.115}$$

Averaging over all particles yields the new rms emittances:

$$\varepsilon'_k = \int dx^4 I'_i(\mathbf{x}) f(x) = \frac{1}{8\pi^2\varepsilon_1\varepsilon_2}\int dx^4 \left|\mathbf{v}'_k{}^{+}\mathbf{U}\mathbf{x}\right|^2 \exp\left(-\frac{1}{2}\mathbf{x}^{\mathrm{T}}\boldsymbol{\Xi}\mathbf{x}\right). \tag{2.116}$$

Similar to Eq. (2.35) a coordinate transform, $\mathbf{y} = \mathbf{V}^{-1}\mathbf{x}$, reduces matrix $\boldsymbol{\Xi}$ to its diagonal form. That results in

$$\varepsilon'_k = \frac{1}{8\pi^2\varepsilon_1\varepsilon_2}\int dy^4 \left|\mathbf{v}'_k{}^{+}\mathbf{U}\mathbf{V}\mathbf{y}\right|^2 \exp\left(-\frac{1}{2}\mathbf{y}^{\mathrm{T}}\hat{\boldsymbol{\Xi}}\mathbf{y}\right), \tag{2.117}$$

where matrix $\hat{\boldsymbol{\Xi}}$ is determined by the beam initial emittance in accordance with Eq. (2.28). Taking into account Eqs. (2.36) and (2.37), we finally obtain

$$\varepsilon'_k = \frac{1}{2}\mathbf{v}'_k{}^{+}\mathbf{U}\boldsymbol{\Sigma}\mathbf{U}^{\mathrm{T}}\mathbf{v}'_k, \quad k = 1, 2. \tag{2.118}$$

For initially uncoupled beam characterized by β_x, β_y, α_x, and α_y at the injection point that yields

$$\begin{aligned} \varepsilon_1{}' &= \varepsilon_1 A_{11} + \varepsilon_2 A_{12}, \\ \varepsilon_2{}' &= \varepsilon_1 A_{21} + \varepsilon_2 A_{22}, \end{aligned} \tag{2.119}$$

where

$$\begin{aligned} A_{11} &= \frac{1}{2}\left(\frac{\beta_x}{\beta_{1x}}\left[(1-u)^2 + \alpha_{1x}{}^2\right] + \frac{\beta_{1x}}{\beta_x}\left[1 + \alpha_x{}^2\right] - 2\alpha_{1x}\alpha_x\right), \\ A_{12} &= \frac{1}{2}\left(\frac{\beta_y}{\beta_{1y}}\left[u^2 + \alpha_{1y}{}^2\right] + \frac{\beta_{1y}}{\beta_y}\left[1 + \alpha_y{}^2\right] - 2\alpha_{1y}\alpha_y\right), \\ A_{22} &= \frac{1}{2}\left(\frac{\beta_y}{\beta_{2y}}\left[(1-u)^2 + \alpha_{2y}{}^2\right] + \frac{\beta_{2y}}{\beta_y}\left[1 + \alpha_y{}^2\right] - 2\alpha_{2y}\alpha_y\right), \\ A_{21} &= \frac{1}{2}\left(\frac{\beta_x}{\beta_{2x}}\left[u^2 + \alpha_{2x}{}^2\right] + \frac{\beta_{2x}}{\beta_x}\left[1 + \alpha_x{}^2\right] - 2\alpha_{2x}\alpha_x\right) \end{aligned}$$

and β_{1x}, β_{1y}, β_{2x}, β_{2y}, α_{1x}, α_{1y}, α_{2x}, α_{2y}, and u are the generalized Twiss parameters of the ring at the injection point. For uncoupled ring optics, $\beta_{1y} = \beta_{2x} = \alpha_{1y} = \alpha_{2x} = u = 0$, we obtain the well-known expression:

$$\begin{aligned}\varepsilon_x{}' &= \frac{1}{2}\varepsilon_x\left(\frac{\beta_x}{\beta_{1x}}\left[1+\alpha_{1x}{}^2\right]+\frac{\beta_{1x}}{\beta_x}\left[1+\alpha_x{}^2\right]-2\alpha_{1x}\alpha_x\right),\\ \varepsilon_y{}' &= \frac{1}{2}\varepsilon_y\left(\frac{\beta_y}{\beta_{2y}}\left[1+\alpha_{2y}{}^2\right]+\frac{\beta_{2y}}{\beta_y}\left[1+\alpha_y{}^2\right]-2\alpha_{2y}\alpha_y\right).\end{aligned} \tag{2.120}$$

One can see that the emittance growth is absent only if the Twiss parameters of injected and circulating beams are equal.

2.2 Linear Optics Measurements

Linear optics measurements have played an important role for improvement of the Tevatron complex performance. Accurate knowledge of the ring and transfer line optics resulted in the significant reduction of the emittance growth for beam transfers and increased the acceptances of the rings and transfer lines with subsequent reduction of the beam loss at transfers and in the course of other operations. In the case of Tevatron, it resulted in a decrease of the beta-functions at the IPs (with subsequent luminosity increase), helped to maintain equal luminosities at the two experiments, was instrumental in locating magnet misalignments and keeping the machine stable over long periods of time, and provided valuable input for various simulations, including the simulation of beam–beam effects, optimization of helical orbits, and collimation. In the case of Debuncher and Accumulator, an accurate knowledge of magnet focusing allowed us to modify machine optics so as to maximize acceptances of the machines and to improve performance of stochastic cooling systems (see Chap. 7). A number of methods and software tools were developed to streamline the process of data acquisition, processing, and analysis. All methods that were employed for the Tevatron linear optics measurements rely on the beam position information provided by the Tevatron BPM system (see Chap. 9). Later these methods were used to build accurate optics models for Debuncher, Accumulator, and Recycler.

Historically, the first method used for optics measurements in Run II was based on the analysis of orbit response data generated by a small number (usually four) of dipole correctors and an energy change [9]. An automated software program has been used for data acquisition. It makes the corrector current change and records the resulting orbit difference with respect to the nominal orbit (hence, we use the term *differential orbit measurement* to describe the method). The generated orbits were then compared with the model prediction, and the model was corrected to minimize discrepancies between measurements and the model. Later more sophisticated software tools were built for analysis of multiple differential orbits and an automatic correction of optics model for circular machines. Unfortunately this software cannot be used effectively for transfer lines because it requires much more data, and

such data acquisition is time prohibitive for the most transfer lines of the Tevatron complex.

The idea of the method is based on an excitation of betatron wave with a single dipole corrector kick. For a transfer line, the wave is propagating downstream of the corrector and corresponding beam displacement is

$$x(s) = \theta\sqrt{\beta(s)\beta(s_0)}\,\sin\left(\mu(s) - \mu(s_0)\right). \tag{2.121}$$

For a ring the closed orbit displacement is

$$x(s) = \frac{\sqrt{\beta(s)\beta(s_0)}}{2\sin\left(\pi Q\right)}\theta\cos\left(|\mu(s) - \mu(s_0)| - \pi Q\right). \tag{2.122}$$

Here Q is the betatron tune, θ is the corrector kick, β and μ are the betatron function and phase, and index 0 labels the corrector location. A focusing error results in an unaccounted kick with angle

$$\delta\theta = \Delta K l\, x,$$

where $\Delta K l$ is the error in the integrated quadrupole strength and x is the orbit displacement. That affects the phase and amplitude of betatron motion relative to the computer model predictions. As one can see from the above equation, the value of the kick is proportional to the trajectory displacement in the quadrupole, and therefore a single differential orbit has suppressed sensitivity to focusing errors in the vicinity of locations where the differential orbit crosses zero. Therefore, at least two differential orbits (for each plane) are needed to sense all focusing errors. In optimum the betatron phases of these orbits should be shifted by $(n + 1/2)\ \pi$, although deviations from optimum in the range of $\pm\pi/4$ do not introduce large penalty to the measurement accuracy. In the case of energy change, the beam displacement is proportional to the corresponding plane dispersion. This response is "orthogonal" to responses of orbit bumps; it additionally limits possible corrections of quadrupole strength and therefore is extremely helpful in finding an actual machine model. Its usefulness is greatly amplified by limited accuracy of BPM measurements related to the BPM noise and errors of BPMs differential response. Although the noise in principle (but not always in practice) can be reduced by increasing number or duration of measurements, the BPM differential sensitivity is a significant factor affecting the accuracy of the measurements and has to be specially addressed.

The most detailed optics models of rings and transfer lines were built using the OptiM code [10]. The models have included all optics-related elements: magnets, linear and nonlinear correctors, BPMs, profile monitors, aperture limitations, stochastic cooling tanks, etc. All important properties of magnets such as the dependence of strength on the current and nonlinearities derived from magnetic measurements have been also included in the models. Locations of all elements

have been cross-checked with machine alignment data. However, comparison of model predictions with measurements showed significant discrepancies pointing out that there are non-negligible errors in the focusing properties of magnets. To address it we added into the model the pseudo-quadrupoles (and if necessary the pseudo-skew-quadrupoles) near each quadrupole which adjustments allowed matching the model to the measurements. Although in the most of cases we do not know origins of focusing errors, such approach allowed us to build credible machine models accurately describing ring or transfer line focusing.

There is significant difference in optics measurements for transfer lines and circular machines. In a ring the beam is permanently present, and therefore an accumulation of multiple BPM measurements can be done fast and accumulation of large datasets is not a problem. In this case multiple correctors are used for optics measurements. That creates a redundancy in the data allowing us to make an automated data analysis resulting in a high-accuracy optics model. Accumulation of differential orbit data for a transfer line happens much slower—once or twice per minute. Usually to achieve a minimally required statistical accuracy, at least four measurements are required for each corrector. Taking into account that at least four correctors and an energy change are required and the reference orbit has to be measured before and after the measurement, one obtains a minimum measurement time of about 15 min. Usually measurements are done for both polarities of differential orbits resulting in 30 min to an hour to acquire good dataset for a transfer line. Therefore, the datasets for transfer lines do not have sufficient redundancy for an automatic data analysis and data are analyzed manually, i.e., a person assigns focusing errors to quads. Normally it takes from a few hours to a day to build a transfer line optics. That is a good compromise between time spent for measurements and the data analysis. Due to lack of data and limited human ability to digest still quite large datasets, the accuracy of obtained optics model is not the same good as for rings. However, we found it adequate to the requirements of Tevatron complex transfers. Together with absolute and differential orbits the software records a beam intensity signals for each BPM. Changes in the beam intensity correlated with beam displacement allow one to identify places of potential beam scraping and, taking into account that the measurements are performed for both polarities of each kick, to formulate suggestions for changes of the beam orbit in the transfer line.

Note also that as part of the effort to improve the status of the accelerator complex, three databases were created: (1) the lattice repository which keeps the optics files, (2) the magnet database which keeps the results of magnetic measurements, and (3) the survey database which keeps results of machine surveys and alignment.

2.2.1 Linear Optics Optimization and Linear Optics Measurements for Transfer Lines

At the Run II beginning improvements of optics for transfer lines was much more important problem than optics improvements for circular machines. There were three main reasons: first, historically much more attention was paid to the optimization of optics for circular machines; second, most transfer lines are between rings belonging to different departments and therefore their ownership was not uniquely determined; third, long transfer lines historically were split into a few segments and optics was designed and supported independently for each segment. The Run II clearly demonstrated that resolving transfer line optics is the same challenging as resolving circular machine optics, and therefore the same attention has to be paid to the transfer line optics design and commissioning. There are ten transfer lines in the Tevatron complex: (1) linac to Booster, (2) Booster to MI, (3) Main Injector to antiproton production target, (4) antiproton production target to Debuncher, (5) Debuncher to Accumulator, (6) Accumulator to Main Injector, (7, 8) two lines (proton and antiproton) from Recycler to Main Injector which are also used for Main Injector-to-Recycler transfers, and (9, 10) two lines (proton and antiproton) from Main Injector to Tevatron. There are also transfer lines for neutrino experiments and experiments with fixed targets which are not discussed here. For almost all lines optics was redesigned to improve transport quality. Optics for all of them was measured and if necessary corrected to meet the design intent.

At the Run II beginning the most outstanding optics problems were related to the Accumulator-to-Main Injector transport of antiprotons at 8 GeV. It is the longest and most complicated transfer line in the Tevatron complex. Therefore, resolving its optics problems is considered here in detail. Optics problems of other transport lines were similar and the same approach and software were used to address them. If not directly mentioned, the discussion in the rest of this section is about the Accumulator-to-Main Injector transport.

The total length of beam transport from Accumulator to Main Injector is more than 900 m. Almost 600 m of this line is also used for the 120 GeV proton beam transport from Main Injector to the antiproton production target. Large difference in the energies results in that the magnetic fields of the low-energy transport are dominated by the residual magnetic field of the magnets. At the Run II beginning the situation was so critical and uncertain that the question of building a new 8 GeV line was seriously discussed. However, the differential orbit measurements proved that the line optics is sufficiently reproducible and the decision was made to redesign and tune optics of the existing line. The main objectives for new optics design were as follows: (1) maximize the line acceptance for existing aperture limitations, (2) match transfer line optics to the optics of both rings including both vertical and horizontal dispersions, and (3) minimize (or better eliminate) any hardware work in the tunnel. The transfer line has 63 quadrupoles connected to 35 quadrupole families. Large number of quadrupole families offers considerable freedom for optics design, but at the same time it greatly complicates finding a good

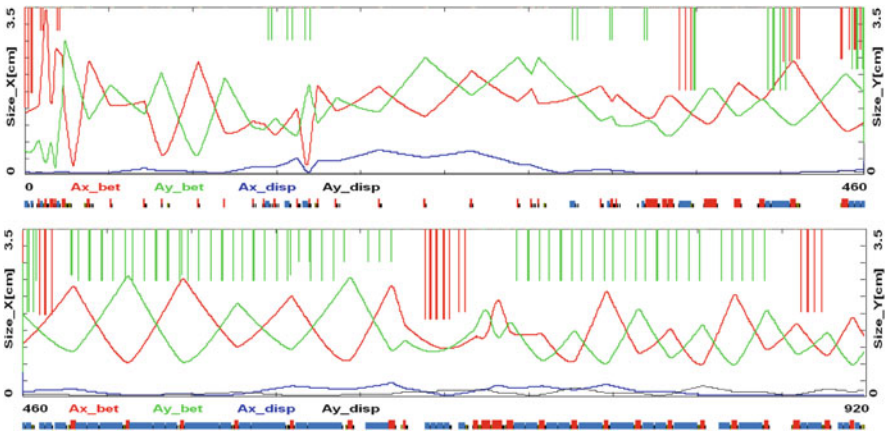

Fig. 2.1 Calculated beam envelopes of the entire Accumulator-to-Main Injector transport for the beam emittances equal to the line normalized acceptances 48 and 42 mm mrad for horizontal (*red*) and vertical (*blue*) planes, correspondingly. *Top* and *bottom* plots present the envelopes for the first and second halves of the beamline. *Blue* and *black* curves present contributions to the beam size coming from the momentum spread of $\Delta p/p = 6 \times 10^{-4}$ corresponding to 2.5σ of typical momentum spread of extracted beam. *Vertical lines* show aperture limitations for horizontal (*red*) and vertical (*green*) planes. *Squares* below the plots present locations of dipoles (*blue*) and quadrupoles (*red*)

solution. Existing aperture limitations were one of the major complications. It forced us to minimize the beta-functions at the aperture limitations and, consequently, yielded an increase of beta-functions in their vicinity and made optics irregular. Although the split of quadrupoles into families was far from optimal, a satisfactory solution was found. Figure 2.1 presents calculated beam envelopes through the entire transport line for the final choice of beamline optics. The horizontal dispersion and both beta-functions were matched to the ring dispersions and beta-functions. The existing quadrupole families did not allow matching the vertical dispersion, but the line optics was designed to minimize the vertical dispersion leakage from the line. Together with a small value of extracted beam momentum spread, it resulted in a negligible contribution of vertical dispersion mismatch to the emittance growth, thus, allowing us to achieve good transfer line performance without reconnecting the quadrupole families.

The optics measurements have been based on the differential orbit measurements. Normally the measurements were performed with reverse protons, where the proton beam is sent from Main Injector to Accumulator. Figure 2.2 presents a typical measurement consisting of five differential orbits representing responses to two horizontal and two vertical correctors and an energy change. To make sure that the BPM response is not affected by beam scraping, the measurements were acquired for positive and negative excitations. It also improves statistical accuracy. Curves present the model predictions after the model was fitted to the data. *X*–*Y* coupling in the line is sufficiently small, and therefore the cross-plane responses for the corrector excited orbits are not presented in the figure. Variations of BPM

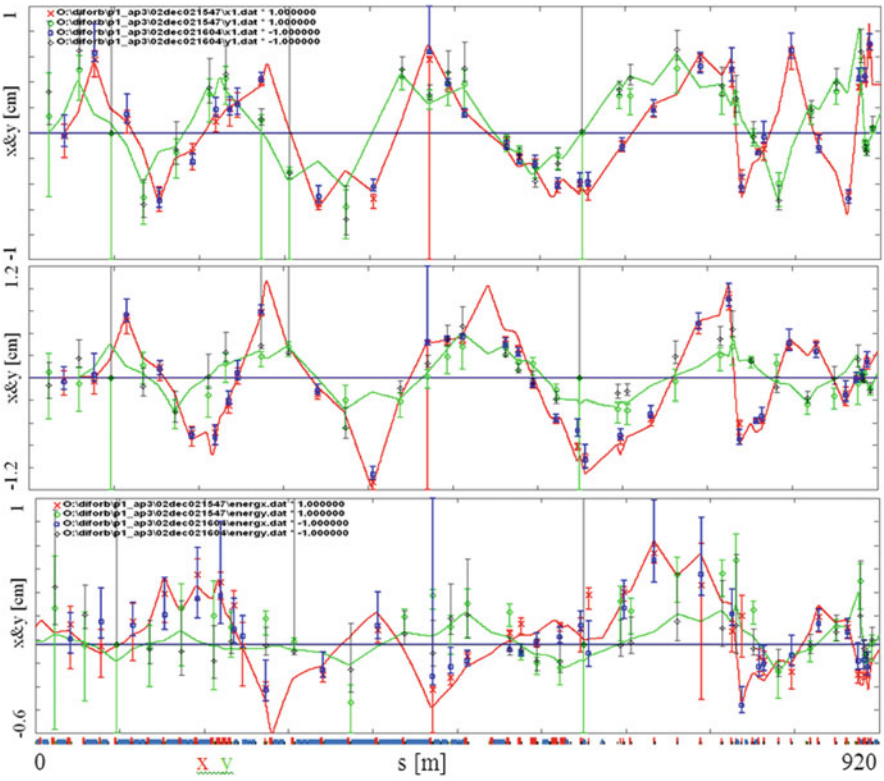

Fig. 2.2 Typical differential obit measurement for the Accumulator-to-Main Injector beam transport and its fitting by refined optics model: *red* and *blue* dots present a horizontal response to a horizontal corrector and *green* and *black* dots a vertical response to a vertical corrector. *Blue* and *black* dots represent inverted values of data acquired with negative corrector excitation. Short error bars present a standard deviation and long error bars present a maximum deviation from the mean value of 3 measurements. Long error bars which cross the entire plot show BPMs with an error status which potentially can have incorrect measurements

differential response significantly complicate finding good solution. In this case the beam displacement reported by a BPM is proportional to the actual displacement but not necessarily with correct coefficient of proportionality.[5] Therefore, the best fit to the data usually yields too large corrections to quadrupole focusing, and,

[5] Experience gained with the upgrade of electronics of Tevatron BPMs carried out in 2004 proved that before the upgrade the major contribution to variations of differential BPM response was related to imperfections of electronics. After the upgrade the spread of variations was reduced from ~10 to ~1 %. Contribution coming from nonlinearity of differential BPM response with coordinate related to the geometry of BPM was much smaller. The imperfection of electronics looks the most probable reason for variations of differential BPM response for the transfer line BPMs.

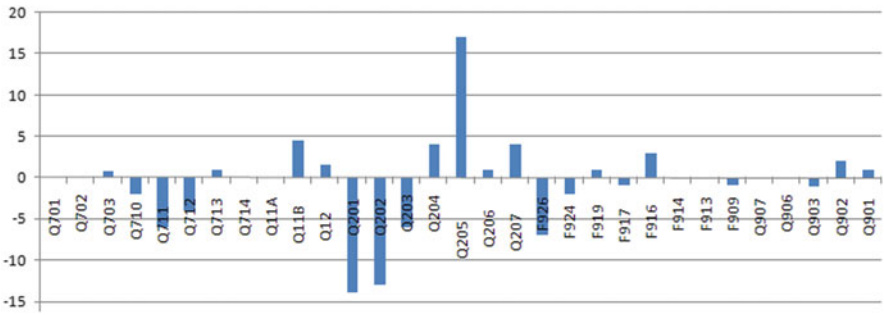

Fig. 2.3 Corrections (in %) to quadrupole power supplies currents for Accumulator-to-Main Injector beam transport. The 120 GeV beamline includes quadrupoles from Q701 to Q207. The rest of the line operates at 8 GeV only

consequently, the model represents poor the actual line focusing. To address this problem we put more trust to the BPMs in which measurements are close to zero, and, consequently, are weakly affected by errors of differential beam response. Normal functioning of these BPMs is verified by measurements with nonzero beam displacements. They come from another corrector of the same plane. Normally optics model update/correction proceeds from the transport line beginning to its end. One corrects quadrupole focusing iterating between different differential orbits. A few rounds of corrections are usually required before a satisfactory match to the measurements is found. Figure 2.3 presents corrections to the power supply currents required to match the model to the differential orbit measurements. One can see significantly larger corrections to the quadrupoles operating both for 8 and 120 GeV transport. Although corrections to quadrupole focusing obtained with this procedure are not unique and do not represent actual errors of the beam transport, they allow one to get an optics model describing the line focusing with satisfactory accuracy. Usually we use the first two correctors of a transfer line, but it does not excite differential orbit in the first quadrupole, and therefore focusing errors of the first quadrupole (closest to Main Injector) are invisible. It can be resolved by an excitation of differential orbit in Main Injector, but it makes both measurements and data analysis more complicated. An upgrade of the transfer line BPM electronics carried out in 2006 made possible accurate position measurements with antiprotons. That allowed us to carry out differential orbit measurements with antiprotons [11]. The measurements were almost not invasive, and because they used antiprotons moving in the opposite to protons' direction, they pointed out a focusing error of the quadrupole closest to the Accumulator (Q901). That resulted in a further improvement of transport quality.

The turn-by-turn measurements of transverse beam sizes of injected antiproton beam offer an independent measurement of the beamline optics. Such measurements became available later in the run when the ion profile monitor (IPM) was commissioned for operations with antiprotons (see Chap. 9). The beam sizes oscillate at the double betatron frequency corresponding to observed frequencies

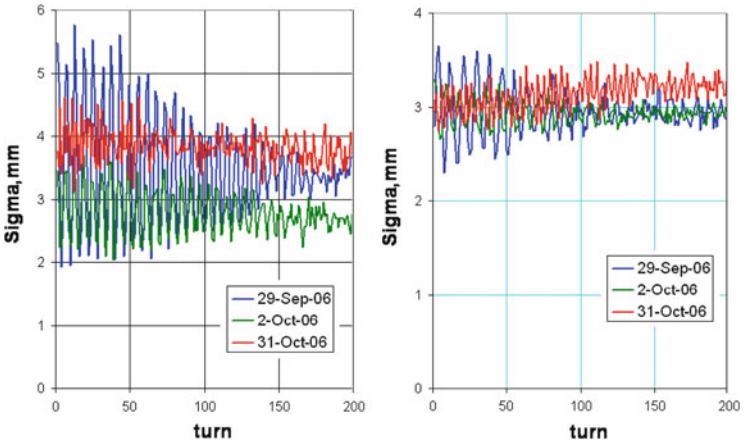

Fig. 2.4 Main Injector IPM measurements of the transverse beam size oscillations at injection. *Left* and *right* plots show horizontal and vertical oscillations, correspondingly, before the optics matching (*blue*), after first correction (*green*), and after second correction (*red*)

$2\nu_x \sim 0.12$ and $2\nu_y \sim 0.16$. Figure 2.4 presents an improvement of IPM signals with improving optics match [11]. As one can see in Fig. 2.4, there was a considerable mismatch between Accumulator and Main Injector before correction. However, the emittance increase was not as bad as the beta-function mismatch because the emittance growth is proportional to $(\Delta\beta/\beta)^2$. The estimate can be obtained from the well-known formula, describing the emittance growth due to optics mismatch:

$$\varepsilon' = \frac{\varepsilon}{2}\left(\frac{\beta_1}{\beta_2}\left[1+\alpha_2{}^2\right]+\frac{\beta_2}{\beta_1}\left[1+\alpha_1{}^2\right]-2\alpha_1\alpha_2\right) + \frac{\sigma_p{}^2}{2}\left(\beta_2\left(D_0'-D_1'\right)^2+2\alpha_2\left(D_0'-D_1'\right)\left(D_0-D_1\right)+\frac{\left(D_0-D_1\right)^2}{\beta_2}\left(1+\alpha_2{}^2\right)\right), \tag{2.123}$$

where β_1, α_1, D_1, and D_1' are the beta- and alpha-functions, the dispersion and its derivative for the incoming beam, and β_1, α_1, D_1, and D_1' are the beta- and alpha-functions of circulating beam. Expending this equation for the case of small quadrupole betatron oscillations and taking into account that $\Delta\beta/\beta \approx 2\Delta\sigma/\sigma$, one obtains

$$\frac{\delta\varepsilon}{\varepsilon} \approx \frac{1}{2}\left(\frac{\Delta\beta}{\beta}\bigg|_{\max}\right)^2 \approx 2\left(\frac{\Delta\sigma}{\sigma}\bigg|_{\max}\right)^2. \tag{2.124}$$

For the data presented in Fig. 2.4, it yields $\delta\varepsilon_x/\varepsilon_x \approx 0.5$ (0.03) and $\delta\varepsilon_y/\varepsilon_y \approx 0.07$ (0.015), correspondingly, before and after the final correction.

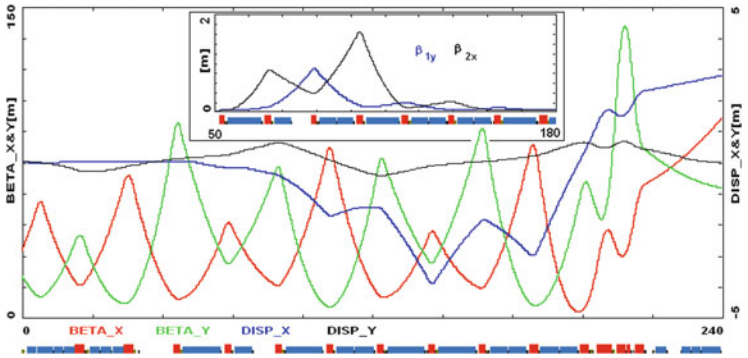

Fig. 2.5 Beta-functions and dispersions for proton transport from Main Injector to Tevatron. *Inset* presents auxiliary beta-functions of coupled motion, β_{1y} and β_{2x}

Standardization of hysteresis protocol and two sets of power supplies (one for 8 and another for 120 GeV) have been required to achieve desired reproducibility of beam transport. However, its seasonal variations still were present in the Accumulator-to-Main Injector line. Other transfer lines operate at the energies which they were designed for. Consequently, they have better reproducibility and have not required additional tuning since the time when their optics was corrected.

As it was already mentioned, Run II inherited a number of problems rooted in Tevatron history. One of them was a vertical dispersion mismatch in the Main Injector-to-Tevatron proton beam transport line. Existing quadrupole powering did not allow matching of vertical dispersion. An independent powering for a string of 7 quadrupoles could address the problem, but it required new power supplies and additional cabling. A simple solution of the problem implied rolling 4 of 7 quadrupoles of the string by small angles. The angles and quadrupole strengths were adjusted to make the uncoupled transport through the string (see inset in Fig. 2.5) and to match beta-functions and dispersions. This line is also used for the antiproton transport described above and the proton beam transport to the antiproton production target. Uncoupled transport through the string simplified their optics correction.

Note that in most cases the emittance increase of about 5 % is acceptable. In this case Eq. (2.124) yields a required transfer line optics match $\Delta\beta/\beta \leq 0.3$. The requirements to optics of circular machines like Tevatron, Debuncher, and Accumulator are much stricter, and therefore a usage of the multi-corrector automated algorithm described in the next section has been absolutely essential to address their optics issues.

2.2.2 Linear Optics from Closed Orbit

The simplified differential orbit method described above was used in 2003 for measurement and correction of the injection and collision lattices for Tevatron. The most spectacular result was achieved for the collision optics—it was discovered that due to the significant (up to 1 %) gradient errors in the final focus quadrupoles, the β^* values were about 30 % larger than the design. Correction of these errors resulted in an immediate increase of the luminosity. However, the data analysis was tedious and the results still were not sufficiently accurate. It was recognized that both more accurate and better-automated methods are required. The development followed two directions: extension of the differential orbit technique discussed here and analysis of the turn-by-turn data discussed in the next section.

Response matrix fitting is a well-known method of calibrating the machine optics. It was first suggested at SLAC [12] and then it was used at NSLS [13] for X-ray ring analysis. Today the method is widely used at many accelerators around the world [14]. At the Tevatron, a modification of the response matrix fitting software developed at Argonne National Laboratory for the Advanced Photon Source (APS) [15] has been used.

The response matrix fitting program SRLOCOFitting [15] written in Tcl/Tk has an extensive graphical user interface, and uses SDDS toolkit [16] for data processing. The code was developed to calibrate the APS model and to provide data for beta-function correction. Coupling correction was not an issue at the APS; therefore, the calculations were limited to the uncoupled case. On the contrary, coupling of horizontal and vertical betatron motion was an important for the Tevatron; therefore, existing analyses had to be expanded to a fully coupled motion. Another important modification was the addition of dispersion to the fit. This allowed us to resolve two issues. First, addition of dispersion adds a constraint on the quadrupole gradients, removing the degeneracy between in-phase quadrupoles. Second, the dispersion can be used to calibrate average gain of BPMs, which otherwise would be a degenerated value. Technically, dispersion is treated as a column of the response matrix. A number of other minor code modifications have been made to ensure that the software could be used with other Fermilab accelerators.

The Tevatron ring has 110 correctors and 118 BPMs in each plane. The response matrix measurement procedure was fully automated and used the following procedure: each steering magnet was excited first with positive current and then with negative current. At each value of current, the orbit was measured 25 times. The total response to the steering magnet excitation was the average positive orbit minus the average negative orbit. The output of the measurement program was an SDDS file containing average orbit responses and their rms deviations in a format readable by SRLOCOFitting. The dispersion measurement was done by scanning the RF frequency, measuring orbit at five points, and fitting a straight line at each BPM. It resulted in an improvement of measurement accuracy. Acquisition of the full response matrix required approximately 2 h of beam time. However, it was

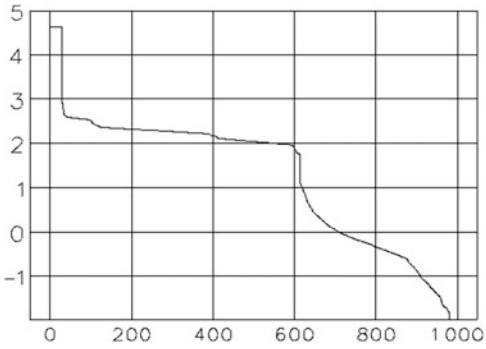

Fig. 2.6 Singular values (logarithmic scale) of the Tevatron response matrix derivative

determined that a good quality fit could be obtained with a smaller dataset, and in normal operations the response matrix was measured using 60 correctors, which took less than 1 h.

The fit produced values of the following variables: quadrupole gradient errors, quadrupole tilts, corrector calibration errors, corrector tilts, BPM gains and BPM tilts, and energy shift due to corrector changes. The total number of unknown variables was about 1,000. Since the LOCO fitting procedure is based on the computation of pseudo-inverse of the response matrix derivative using singular value decomposition, important information is contained in the spectrum of singular values. Figure 2.6 presents a typical plot of the singular values for the Tevatron collision optics. The SVD cutoff was typically chosen at 1, which corresponds to 600–650 singular values.

The main factor limiting accuracy of the LOCO fit is the resolution of the beam position measurement. The BPMs have the resolution of about 10 μm for a single measurement. Besides, the beams oscillate at low (~10 Hz) frequency with the amplitude of about 50 μm. Averaging over 25 measurements has been applied to mitigate the effect of slow oscillations. The overall accuracy of the orbit measurement was then about 15 μm. Figure 2.7 shows the rms difference of the measured orbit and the modeled orbit after the fit for each BPM. In this case, 30 horizontal and 30 vertical orbits were used and the average error was ~14 μm which is close to the orbit measurement accuracy.

The precision of the orbit fitting sets the accuracy of gradient error determination, which in our model is 10^{-3} for the arc quads and 10^{-4} for the final focus quads. The corresponding error in beta-function is about 5 %. In Fig. 2.8 the found quadrupole and skew-quadrupole errors are presented for all locations in the Tevatron.

Two locations with large skew-quadrupole component, D16 and A38, have been identified as tilts of the corresponding quadrupoles. These tilts emerged at the magnet assembly and could not be found by alignment measurements from outside of the magnet.

Table 2.1 summarizes the gradient errors for the final focus quadrupoles. As one can see, the difference from the calibration curve obtained by magnetic measurements can be as high as 1 %.

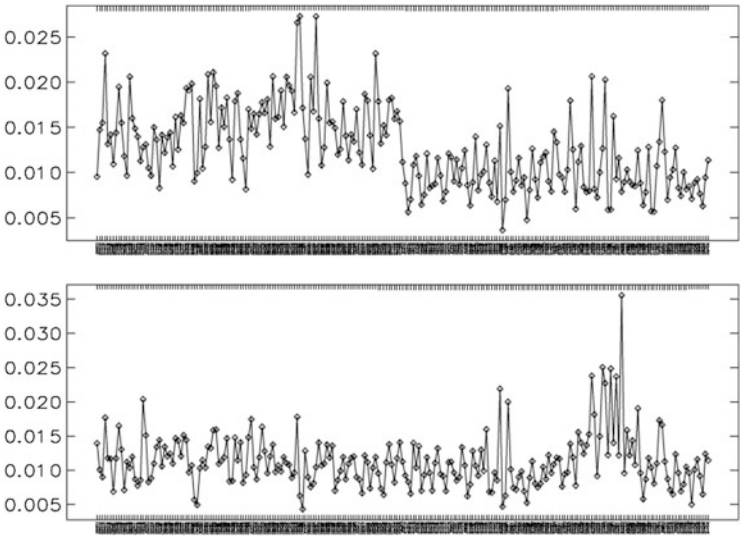

Fig. 2.7 Rms difference (mm) between the measured and modeled orbit vs. BPM name. *Top*, horizontal orbit; *bottom*, vertical orbit

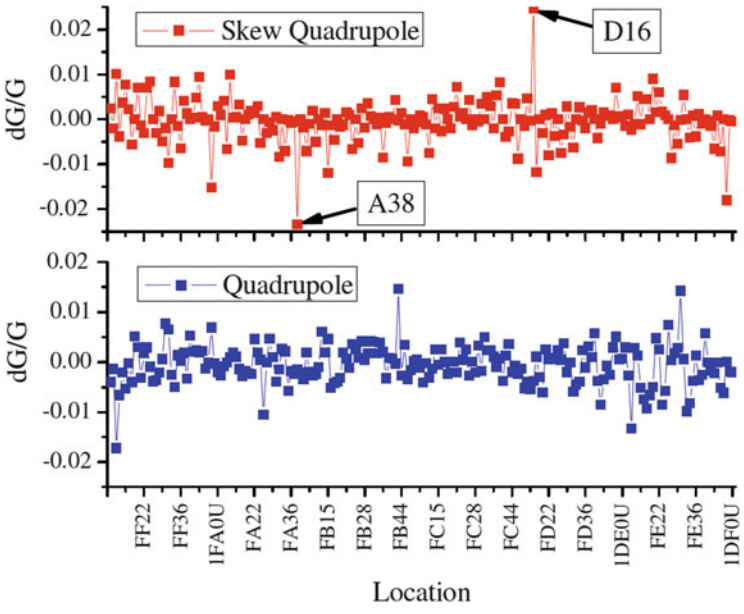

Fig. 2.8 Measured relative quadrupole and skew-quadrupole errors

Table 2.1 Relative quadrupole errors in final focus

Name	Gradient error (10^{-3})
B0Q3	−11.18
B0Q2	−1.87
B0Q3D	−0.09
B0Q3F	−0.47
D0Q3	−9.49
D0Q2	−0.83
D0Q3F	0.24
D0Q3F	−1.84

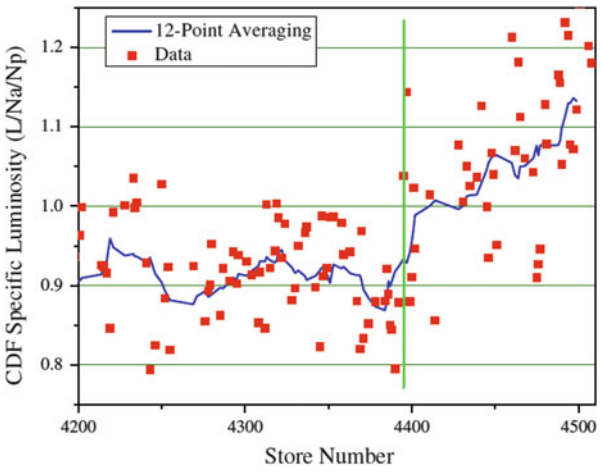

Fig. 2.9 Specific initial luminosity ($L/N_a/N_p$) vs. store number. *Green line* marks the moment when the new optics was put into operation

Based on the knowledge of the lattice details, new collision optics has been implemented in 2005 with the following goals:

1. Eliminate beta-beating in the arcs.
2. Correct the discrepancy in the values of β^* between the two IPs.
3. Decrease the value of β^* from 35 to 28 cm, with an expected gain in luminosity of 11 % (Fig. 2.9). Further decrease of the β^* was not practical because of the growing second-order chromaticity and little gain in luminosity due to the hourglass effect.

Routine optics measurements with LOCO were performed over the entire length of Run II to support collider operations and simulation efforts.

2.2.3 Turn-by-Turn Measurements

Orbit response matrix analysis is a powerful tool that supplied precise information about the Tevatron linear lattice imperfections and errors of BPM calibrations.

However, orbit data acquisition is a lengthy process and certainly could not be performed on a daily basis and especially during acceleration. For this regime, the Fourier analysis of turn-by-turn beam position after a single-turn kick proved to be invaluable. This method is fast and offers information about entire machine optics. In particular it allows fast computation of the resonance driving terms for the sum and difference betatron coupling resonances and the location of coupling sources [17].

The distribution of coupling sources around the ring determines the resonance driving terms (see Sect. 2.1.12):

$$w_{\pm}(s) = -\int_0^C ds' \frac{C_{\pm}(s')}{4 \sin \pi\nu_{\pm}} \mathrm{e}^{-i\nu_{\pm}(2\pi(s-s')/C - \pi \cdot \mathrm{sign}(s-s'))}, \tag{2.125}$$

where $\nu_{\pm} = \nu_x \pm \nu_y$ and

$$C_{\pm}(s) = \frac{\sqrt{\beta_x \beta_y}}{2} \left\{ 2N + R\left[\left(\frac{\alpha_x}{\beta_x} - \frac{\alpha_y}{\beta_y} \right) - i\left(\frac{1}{\beta_x} \mp \frac{1}{\beta_y} \right) \right] \right\} \times \mathrm{e}^{i(\chi_x \pm \chi_y)} \tag{2.126}$$

Here χ_x and χ_y are the periodic phase functions. The functions $w_{\pm}(s)$ are constant in coupling-free regions and experience a discontinuity at the locations of coupling sources. On the coupling resonances $\nu_x \pm \nu_y = \text{integer}$, the functions $w_{\pm}$ are constant. The minimum attainable tune distance is given by

$$\overline{C}_{\pm} = \frac{n_{\pm} - \nu_{\pm}}{\pi} \int_0^C \frac{ds}{C} w_{\pm} \mathrm{e}^{in_{\pm} 2\pi s/C},$$

with $n_{\pm} = \mathrm{round}(\nu_x \pm \nu_y)$. If the kick occurs in the horizontal plane, the Fourier component $Y_j(\nu_x)$ of $y_j(s)$ is related to the values of $w_{\pm}$ at the j-th BPM via the Twiss functions. When the BPM tilts are negligible or already known (e.g., from the LOCO fit), the number of unknown quantities per BPM is reduced to two and one can retrieve the constant value of $w_{\pm}$ in the region between two BPMs from $Y_j(\nu_x)$ and $Y_{j+1}(\nu_x)$ assuming that there are no strong sources of coupling.

Figure 2.10 presents the vertical injection lattice beta-function reconstructed from turn-by-turn data in comparison with the beta-function obtained by LOCO. One can see that agreement between the two methods is good.

Fig. 2.11 presents the values of real and imaginary parts of $w_{\pm}(s)$ measured at vertical BPMs for horizontal kick and at horizontal BPMs for vertical kick.

An application program for the online turn-by-turn data analysis has been integrated into the Tevatron control system. The program fired the kicker, collected the BPM data, computed Twiss and coupling functions, and, finally, computed and applied the needed corrections to the two main skew-quadrupole circuits SQA0 and SQ. The program was used in routine collider operations during every shot setup and proved invaluable for decoupling on the energy ramp. The time needed to

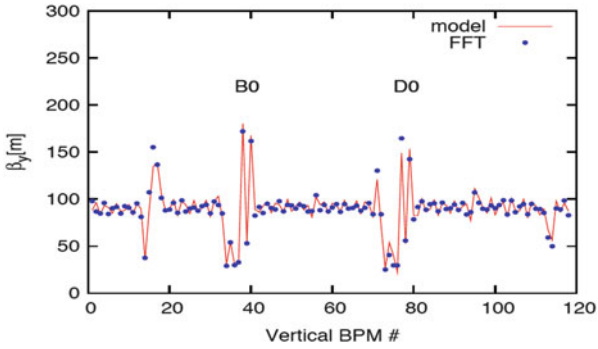

Fig. 2.10 Vertical beta-function at vertical BPMs (injection lattice)

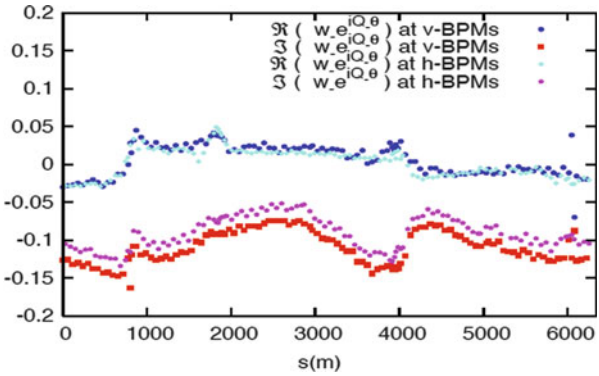

Fig. 2.11 $w_{\pm}(s)$ at vertical BPMs after a horizontal kick (*blue* and *red*), at horizontal BPMs after a vertical kick (*cyan* and *magenta*) as a function of the machine azimuth

retrieve the turn-by-turn data from all Tevatron BPMs was too long for routine use of the method. This limitation could be overcome due to the fact that $w_{\pm}(s) \approx \text{const}$ near the coupling resonances. Since the Tevatron working point at injection ($\nu_x = 20.584$, $\nu_y = 20.574$) is reasonably close to both the difference and the sum resonance, it was possible to use only few BPMs (typically 5 horizontal and 5 vertical) to evaluate the tunes and the functions $w_{\pm}$ at the orthogonal mode BPMs.

2.3 Nonlinear Beam Dynamics

2.3.1 Dedicated Studies of Nonlinear Beam Dynamics in Tevatron

Several important beam studies dedicated to detailed understanding of nonlinear beam dynamics had been carried out at the Tevatron in the late 1980s to early 1990s.

In the E778 beam dynamics experiment, performed in the Fermilab Tevatron, strong nonlinear elements were intentionally added and observations of phase space of nonlinear oscillations were made [18]. For that experiment the Tevatron can be regarded as a linear system on which nonlinearity in the form of 16 sextupole magnets, each of strength S, was intentionally superimposed. The experimental procedure starts with a "needle beam" consisting of some 10^{10} circulating stored protons, to some approximation having essentially the same momentum and to be on the central orbit. Next the same angular deflection D is applied to every particle by a pulsed deflecting magnet. The subsequent beam centroid displacement is sensed for as many as a million turns by beam position monitors (BPM). These measurements are used to generate an experimental Poincaré plot.

To a good approximation, the following equation of motion describes the horizontal particle motion

$$\frac{d^2x}{dt^2} + K(s)x = -\varepsilon(s)x^2. \tag{2.127}$$

Here s is the longitudinal particle coordinate, which advances from 0 to C (the ring circumference). In the course of the experiment the Tevatron tune was about $Q = 19.4$. The anharmonic term in (2.127) is due to sextupole fields of strength $\varepsilon(s)$, proportional to S. That term makes tune of the particle amplitude dependent. Both $K(s)$ and $\varepsilon(s)$ are periodic functions of s with period C. The absence of damping in (1) is valid as the quality factor of these oscillations has a very high value $>10^9$, making this a truly Hamiltonian system. The amplitude (and, thus, the tune) of oscillations can be adjusted by the deflector strength D, so that 20 % of the particles can be trapped in resonance islands. All particles in one of the islands exhibit a tune of exactly 2/5, totally defying decoherence. The resulting BPM signals have been observed to persist for over a minute (approaching a million turns). As an example, Fig. 2.12 shows a "raw" Poincaré plot of transverse beam displacements $x_1(t)$ vs. $x_2(t)$, measured at two positions separated by about one quarter of a betatron wavelength.

The dynamics of a metastable beam of particles "injected" into artificially excited resonance islands in the Tevatron has been further studied in a subsequent experiment [19]. As before, the protons were under the influence of a single dominant nonlinear resonance, caused by the strong excitation of 14 sextupoles in the otherwise nearly linear accelerator. The island location was forced to oscillate at a modulation tune Q_m with an amplitude proportional to the modulation amplitude q:

$$Q(t,a) = Q_{00} + q\sin(2\pi Q_m) + \frac{1}{2}Ua^2. \tag{2.128}$$

Here, the last term represents detuning with amplitude of betatron oscillations a caused by the sextupoles. As in [18], the location and size of the island were adjusted by varying sextupole strengths and the base tune Q_{00} of small-amplitude

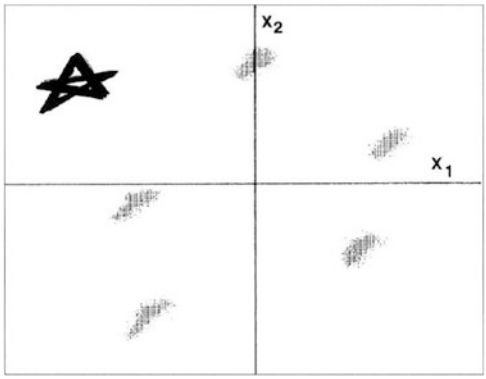

Fig. 2.12 "Raw experimental Poincaré map" exhibiting a metastable state of the accelerator. The logo in the corner of the plot is a demagnified view of the same data with successive points joined by straight lines. The point lands only on every second island, confirming the 2/5 identification [18]

particles. The beam was then allowed to circulate for some 10s to allow transients to decay before data were taken. At 9,000 turns after start of data taking, the tune modulation Eq. (2.128) was turned on by sinusoidal driving two weak quadrupoles. The tune modulation strength and tune, q and Q_m, were linearly ramped for 1 s (about 50,000 turns) and then turned off for the last 0.2 s (some 10,000 turns) of data taking. Figure 2.13 shows the BMP signal during such a chirp. One can clearly see an amplitude modulation of the islands at about 28,000 turns. The persistent signal started dropping dramatically at about 32,000 turns, eventually driving all of the trapped beam out of the resonant island.

The tune modulation trajectory that caused this response is drawn as the dashed line labeled "A" in Fig. 2.14, showing that the signal was lost when the boundary between "amplitude modulation" and "chaos" was crossed. Figure 2.14 also summarizes results from a trajectory labeled "B" that had a very weak constant tune modulation strength $q = 0.000204$, smaller or comparable to realistic operation values. Boundaries found experimentally (circles) and theoretically predicated boundaries between four regions are shown in Fig. 2.14. For the latter ones, the island tune (frequency of small oscillations of the particles trapped in the islands) $Q_I = 0.0063$ was the only free parameter used to adjust the location of these boundaries. A detailed discussion on the theory and explanation of the observations can be found in [18].

The effect of nonlinearity on transverse particle distributions has been studied in yet another beam dynamics experiment [20]. It was concentrated on "stochastic" effects, due to the particle dynamics, that cause "diffusive" evolution of the beam distribution even in the absence of external sources of "noise" or random scattering from residual gas molecules. These effects are studied by adding large nonlinearity to the otherwise comparatively linear machine. At the start of each observation period, a needle-shaped single bunch of some 10^{10} circulating protons was kicked horizontally. This yielded displacement of about 3 mm as observed at a downstream point. The resulting transverse beam profile was repeatedly measured by Flying Wires system every minute or so. During a run of (typical) 30 min duration, each

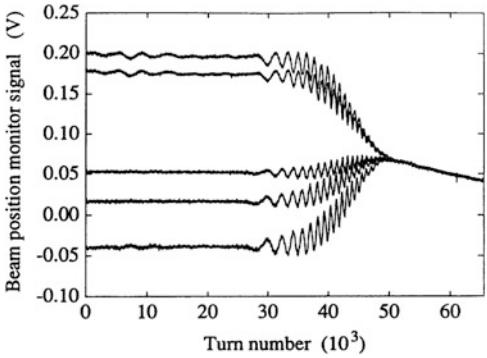

Fig. 2.13 Raw digitized signals of beam position monitor showing a persistent signal and its response to a chirp from (q, Q_m) = (0, 0) to (q, Q_m) = (0.0102, 0.0031). Vertical scale is in volts. Nonzero average initial value is due to a closed orbit offset [19]

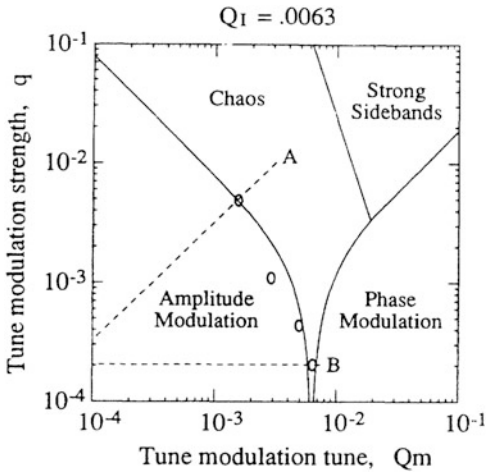

Fig. 2.14 Structure of the tune modulation parameter space (q, Q_m). *A* and *B* correspond to two scans. Four distinct "dynamical phases" are labeled ([19], see in the text)

proton circulates about 10^8 times and executes about 2×10^9 transverse betatron oscillations. The purpose of the kick is to generate a beam in which all the particles are in a region of measurably large diffusion. Individual protons initially oscillate at approximately constant amplitude with damping time equal to many tens of hours, but due to the dynamic diffusion, they start to expand in (initially) void areas of the phase space until they reach a physical aperture (defined by a scraper placed at $x_{\max} = 8$ mm) and get lost. In order to study the influence of resonance, all measurements were performed in the vicinity of the "2/5 resonance" (fractional horizontal tune Q_x close to 0.4).

Contrary to intuition, and unlike multiple scattering, diffusion causes the beam to narrow with time—as shown in Fig. 2.15. That behavior is caused by the sink at the aperture $x_{\max}$ which devours large amplitude particles, reduces the beam intensity, and depletes the tail of the distribution. Time evolution of the beam intensities and full widths, similar to one depicted in Fig. 2.16, was measured at different initial kicks and that allowed to determine the dependence of the diffusion

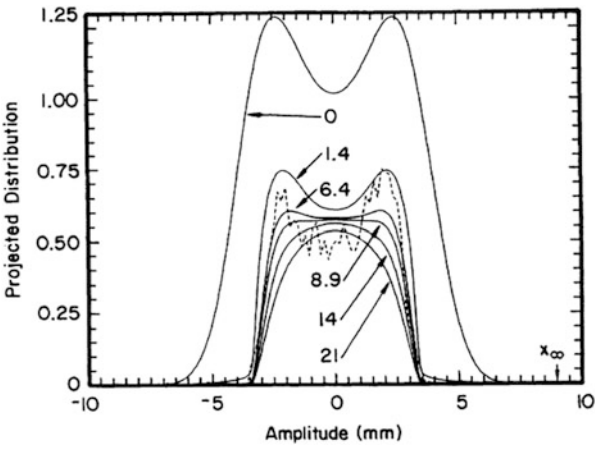

Fig. 2.15 Evolution of the beam profile: the jagged curve is the raw Flying Wire measurement at $t = 6$ min; smooth curves are as predicted by diffusion model. Times (in minutes after hollow beam formation) are indicated [20]

coefficient on the amplitude. Note that similar beam "shaving" phenomena with characteristic intensity decays following $\exp(-t^{1/2})$ law were observed later in the Tevatron Run II when nonlinearity induced by parasitic beam–beam interactions resulted in a significant reduction of a dynamic aperture and beam lifetime degradation—see [21] and discussion in Chap. 8.

2.4 Orbit Motion and Control

Motion of the accelerator components, most notably, quadrupole magnets, results in the beam orbit movements and can lead to a significant deterioration of the collider performance. The mechanism depends on the frequency. At frequencies of betatron sidebands $f_0\,(1-\nu) \approx 19.7$ kHz, fluctuations of the magnetic fields $\delta B(t)$, e.g., due to quadrupole magnet displacements $x(t)$, produce transverse kicks $\delta\theta(t) = \delta B(t)el/Pc = x(t)/F$, where l is the length of the element and F is the focusing length. That leads to the beam emittance growth with the rate of [22]:

$$\frac{d\varepsilon_x}{dt} = \gamma \frac{f_0^2}{F^2} \sum_{k=1}^{N_q} \sum_{n=-\infty}^{\infty} \beta_k S_x(f_0(\nu - n)) \tag{2.129}$$

where f_0 is the revolution frequency, γ is the relativistic factor, ν is the tune, $S_x(f)$ is the power spectral density of the quadrupole motion x, N_q is a total number of quadrupole focusing magnets, and β_k is the beta-function at the k-th quad location. At much lower frequencies, $f \ll f_0$, the kicks lead to a time-dependent displacement of the closed orbit:

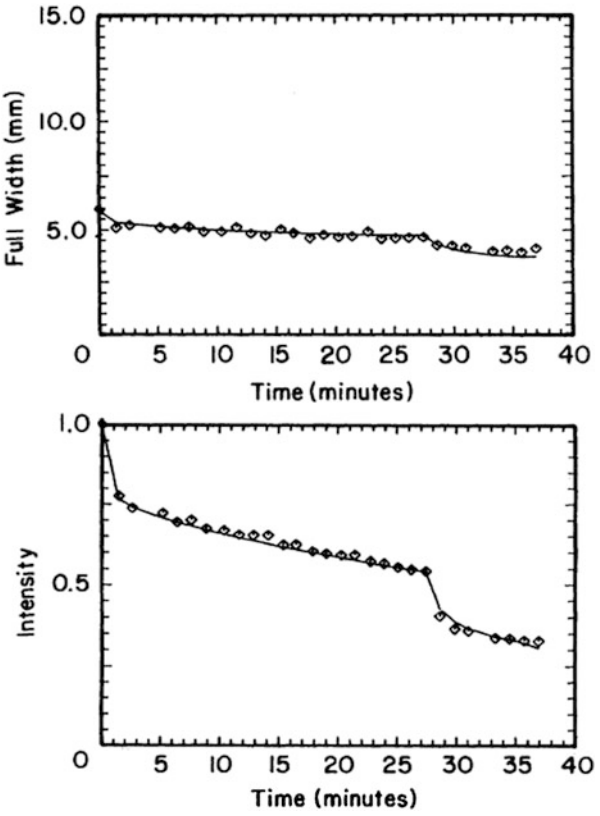

Fig. 2.16 Measured full width and intensity (points) compared to model-derived values (smooth curve). Intensity is normalized to 1 at $t = 0$. The steps at late times are the result of sudden aperture reduction to $x_{\max} = 2.7$ mm [20]

$$X_{\mathrm{COD}}(s) = \frac{\sqrt{\beta(s)}}{2\sin(\pi\nu)} \sum_{k=1}^{N_q} \sqrt{\beta_k(s)}\theta_k \cos\left(\varphi(s) - \varphi_k + \pi\right), \tag{2.130}$$

where s is the location along the ring and $\varphi(s)$, φ_k are betatron phases at the locations of the observation point and at the source of the kth magnet. At very low frequencies, hours to years, the quadrupole magnet displacements are often governed by the "*ATL* law" [23, 24] according to which the mean square of relative displacement dX^2 of the points separated by distance L grows with the time interval between measurements T as

$$< dX^2/dt > \; = A \;\; TL \tag{2.131}$$

where A is a site-dependent constant of the order of $10^{-5\pm1}$ μm^2/(s m) and brackets $<\ldots>$ indicate averaging over many points of observations distanced by L and over all time intervals equal to T. Such a wandering of the accelerator elements takes place in all directions. Corresponding average closed orbit distortion over the ring with circumference C is equal to [25]

$$< X^2_{\mathrm{COD}}(s) > \approx \frac{\beta(s)(\beta_F + \beta_D)}{8F^2 \sin^2(\pi\nu)} ATC \approx \kappa ATC \tag{2.132}$$

where FODO lattice structure is assumed, β_F, β_D are beta-functions at the focusing and defocusing lenses, and numerical coefficient $\kappa \approx 3$ for the Tevatron.

Due to feeddown effects from field non-linearities the Tevatron orbit drifts result in machine optics changes (tunes, coupling, chromaticities). Combined with aperture limitations they lead to increase of beam loss. At the injection energy of 150 GeV when the beams are several mm wide, orbit motion of about a mm leads to losses of the beams at several known places with tight aperture. At the energy of experiment, 980 GeV/beam, beam position in the RF cavities affects stability of high-intensity proton beam, e.g., the power of coherent beam oscillations goes up if the beam is too far off center. Also, oscillations of the RF cavities at synchrotron frequency (85 Hz at 150 GeV and 35 Hz at 980 GeV) are of concern for driving longitudinal emittance growth due to microphonic effects [26]. Large-scale long-term drifts of the orbit can be corrected by dipole correctors, and regular realignment of the magnets—usually during annual shutdown periods—helps to keep the corrector currents under the limit of 50 A.

2.4.1 *Measurements of Betatron Oscillations and Orbit Motion*

Several instruments were used to detect betatron oscillations in the Tevatron (see Chap. 9). The most challenging were direct measurements of natural betatron oscillations at sub-micron level. Several instruments were built for the detecting such oscillations and measurement of their frequency without additional excitation. Various techniques were employed, including 3D-BBQ (direct diode detector baseband tune) measurement system [27] and the digital tune monitor (DTM) which uses 16 bits 100 MHz ADCs for measuring the tunes on a bunch-by-bunch basis [28]. A very high-precision system employing a fast digital scope (Agilent Acqiris, 10bit, 8GS/s) for measurements of the turn-by-turn vertical centroid positions of individual bunches has been devised and used for digitizing signals from the plates of the VB11 BPM in the large vertical beta-function location that translates into better S/N ratio [29]. The system employs variable attenuators for compensating the beam position offset and phase shifters synchronized within 10 ps to minimize common mode. As a result, subtraction of the two signals by an RF hybrid provides about 44 dB of common mode rejection. Figure 2.17 shows 21,400 turn (0.44 s) record of the vertical beam position at the VB11 location.

The FFT of the data reveal significant excess of the signal at the betatron tune over the noise as shown in Fig. 2.18. The rms amplitude of the betatron oscillations is about 110 nm. Note that the amplitude significantly varies from store to store and often is two to three times smaller. That yields some 10–25 nm range of typical rms

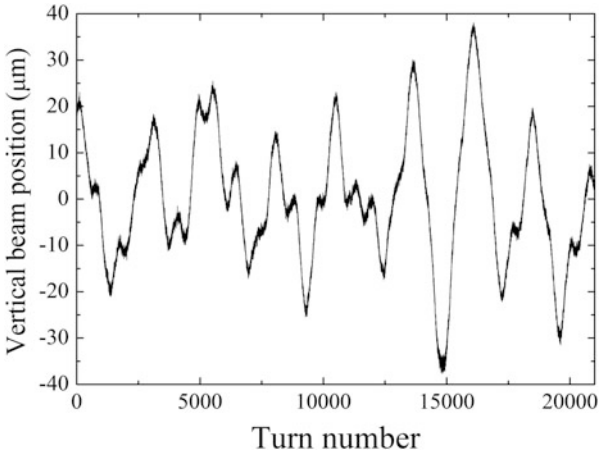

Fig. 2.17 Vertical position of the proton bunch #11 at the beginning of HEP store #6214 (October 2008), measured at the VB11 location with $\beta_y = 900$ m [29]

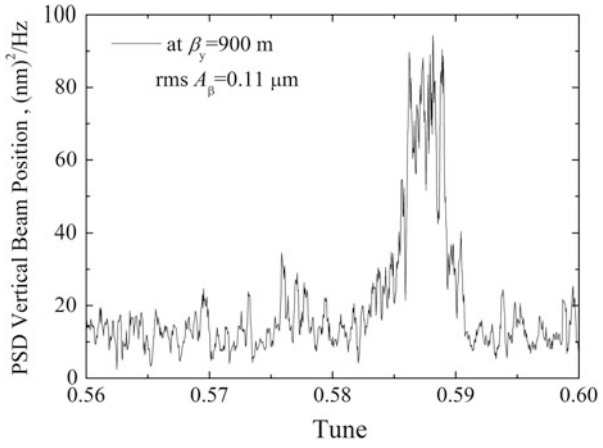

Fig. 2.18 Power spectral density of the vertical betatron oscillations (FFT of the data presented in Fig. 2.17) [29]

betatron motion amplitudes at the average beta-function location with $\beta_y \approx 50$ m. Spectrum of the vertical orbit motion at frequencies 2–1,000 Hz is shown in Fig. 2.19. It scales approximately as $\propto 1/f^3$ and is dominated by the low-frequency beam motion. The strongest lines are the harmonics of 60 Hz main power. The 15 Hz and the 0.45 Hz components can be explained by the effects of the fast cycling Booster synchrotron and the Main Injector on the power distribution systems at FNAL.

At ultralow frequencies, the orbit motion has significant (some 0.1 mm vertical and 0.3 mm horizontal) variation with a period of 12 h, which seems to be associated with Earth tides—see Fig. 2.20 from [30]. The rms of the orbit motion is about 100 μm horizontally and 30 μm vertically. The tide waves are clearly seen in the data from the Hydrostatic Level System (HLS) installed in the MI-8 beamline, the 8 GeV transfer line from the FNAL Booster to the FNAL Main Injector, located within

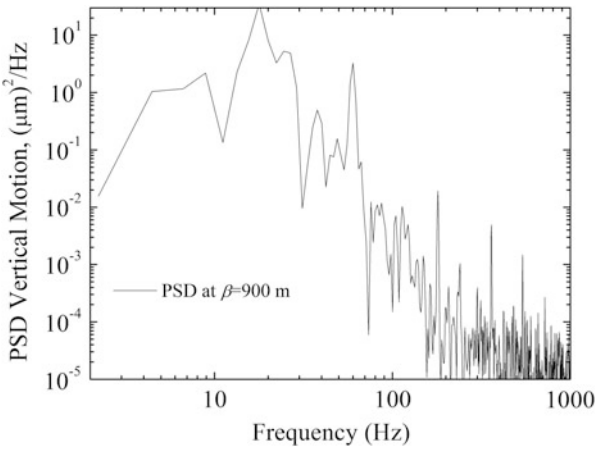

Fig. 2.19 Low-frequency power spectral density of the vertical orbit oscillations [29]

400 m of the Tevatron tunnel. The HLS is described in detail in [24] and consists of 20 submicron resolution water level sensors separated by 15 m from one another. The signal difference for a pair of sensors 135 m apart is plotted at the bottom of Fig. 2.20 and shows some 20 μm peak-to-peak amplitude of the 12 h period component. Slow closed orbit distortions of some 0.5–1 mm rms have been accumulated over 1–2-week intervals and required regular orbit "smoothing," until an automatic orbit stabilization system was introduced in operation in 2005 (see details in Chap. 9) and since then only high-frequency orbit jitter of about 10 μm rms remained.

2.4.2 Magnet and Ground Motion in the Tevatron Tunnel

The low-frequency orbit motion has been found correlated with (caused by) the vibrations of the magnets, particularly, strong focusing near interaction regions. Figure 2.21 from [31] demonstrates strong coherence between quadrupole vibrations and the Tevatron orbit motion, especially at certain frequencies. The coherence spectrum $C(f)$ is defined as

$$C_{xy}(f) = \left| \frac{< S_{xy}(f) >}{\sqrt{< S_{xx}(f) >< S_{yy}(f) >}} \right|, \tag{2.133}$$

where $S_{xy}(f)$ is the cross-correlation spectrum of two signals $x(t)$ and $y(t)$.

One can see that the orbit correlates well with the tunnel floor only at low frequencies ~0.1 Hz, while some excessive but small coherence exists at 2–4 Hz. The beam orbit correlates with the quadrupole magnet motion at frequencies of 0.2–2 Hz.

The closed orbit distortions are caused by the displacements of all magnetic elements along the circumference of the Tevatron. The strong coherence between

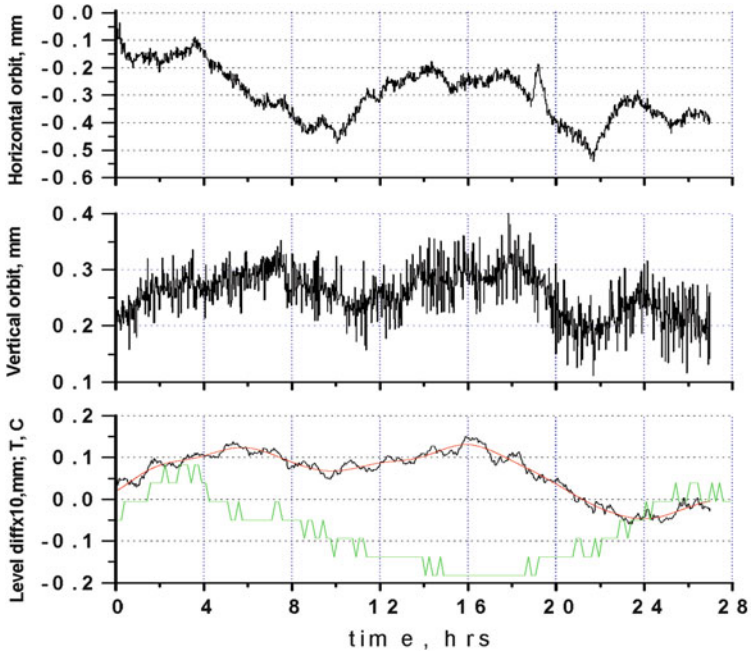

Fig. 2.20 Variation of the Tevatron proton orbits at the F48 location (*top*, horizontal, $\beta_x = 100$ m; *middle*, vertical, $\beta_y = 30$ m); and vertical ground motion as measured in the MI-8 line and temperature (*green* line) measured at the Tevatron sector F48 (both in the bottom plot) during 28 h long collider store #1668 (August 17, 2002)

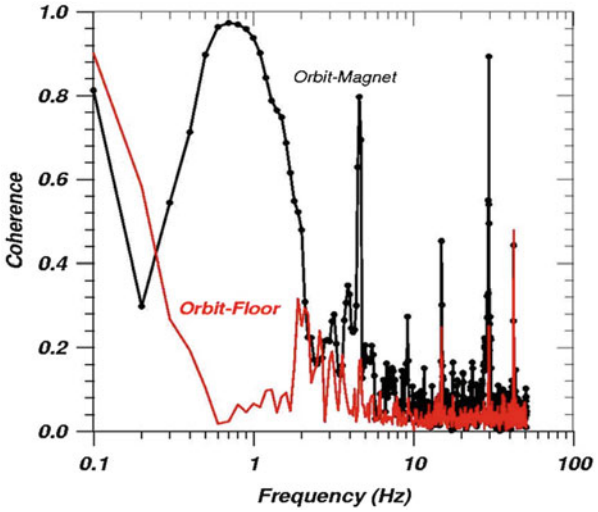

Fig. 2.21 Coherence between signals of the vertical Tevatron beam orbit motion and the F11 magnet vibrations and between the orbit and the tunnel floor (*red line*) [31]

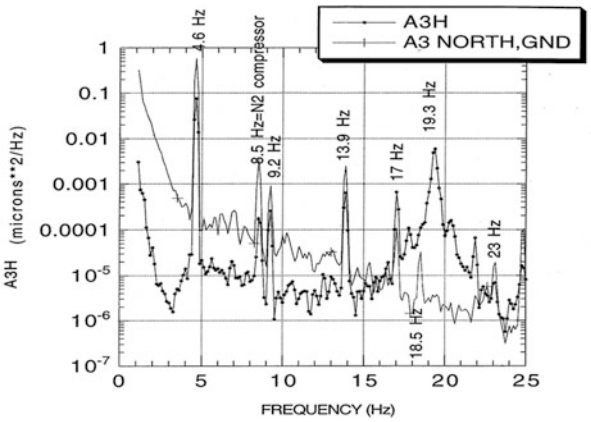

Fig. 2.22 Power spectral density of the A35 quadrupole motion and the ground nearby, from [32]

the magnet and beam vibrations means that there is a common source of vibration along the whole accelerator ring. For example, several remarkable peaks in the orbit–magnet coherence occur at 4.6, 9.2, 13.9 Hz, etc., at the Fermilab site-specific frequencies caused by the Central Helium Liquefier plant operation and well detected everywhere around the ring [32]—see Fig. 2.22.

2.4.3 Slow Diffusion of the Tevatron Tunnel

Analysis of the multiyear Tevatron magnet alignment data shows that in addition to systematic changes due to tides or slow drifts, there is a "random walk" both in time and in space component characterized by the ATL-law of Eq. (4.3) [33].

The alignment system of the Tevatron employs more than 200 geodetic "tie rods" (thick metal rods screwed into the concrete tunnel wall all over the ring and equipped to hold spherical retroreflectors for precise position measurements), each spaced approximately 30 m apart. The positions of the magnets are regularly referenced locally with respect to the "tie rods," while the positions of all the "tie rods" are routinely monitored. The "tie rod" elevation datasets are available for the years of 2001, 2003, 2005, 2006, and 2007. Figure 2.23 shows the change of the elevations $dY(z)$ around the ring accumulated over two intervals—2 years (2003–2005) and 6 years (2001–2007). One can see that longer-term motion has a larger amplitude. The variance $<dY^2(L)> = <(dY(z) - dY(z+L))^2>$ of the elevation difference of the points as a function of the lag (distance between pairs of the measurement points) L has been calculated and averaged over all possible time intervals. That is to say, there are two 1-year intervals (2005–2006, 2006–2007), three 2-year intervals (2001–2003, 2003–2005, 2005–2007), etc., and one for the 6-year interval 2001–2007. The results for the 1-year changes and for the 6-year change are shown in Fig. 2.24. A remarkable difference between the two plots is that 1-year variance scales linearly only up to $L \approx 700$–800 m and does not depend on L beyond that scale, while the 6-year variance grows all the way to distances as

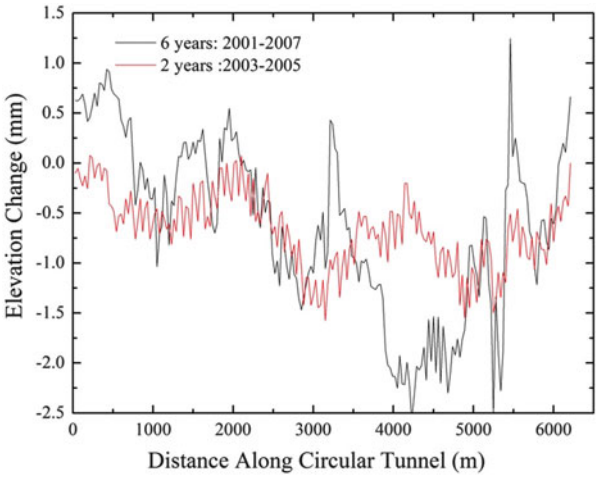

Fig. 2.23 Vertical displacement of more than 200 "tie rods" in the Tevatron tunnel over the period of 2003–2005 and a 6-year period of 2001–2007 [33]

large as 1,800 m. The linear dependence on L is indicative of a significant level of interdependence of the movements of distant points. The calculated variances for all possible time differences can be well approximated by linear fits $<dY^2(L)> = a + bL$ over distances less than 900 m and the slopes (fit parameters b with the error bars) are plotted in Fig. 2.25.

One can see that the variance per unit distance grows with the time interval between the measurements and can be approximated by a linear fit $b(T) = cT$ with $c = 0.153 \pm 0.004$ [mm^2/km/year]. The Tevatron "tie rod" data analysis presented in Figs. 2.24 and 2.25 can be summarized by the ATL law $<dY^2> = ATL$ with coefficient $A_{\text{Tevatron}} = c = (4.9 \pm 0.13) \times 10^{-6}$ μm^2/s/m.

It is to be noted that for small time intervals T the movements of the ground elements are fully uncorrelated if they are separated by a long enough distance $L > L_m$, for example, by more than 800 m for $T = 1$-year intervals as seen in the Tevatron alignment data—see Fig. 2.24—or by more than 120 m for $T = 1$-week intervals as seen in the Tevatron B-sector HLS data [24]. On the basis of these two observations, one can assume that the boundary between totally uncorrelated and the ATL-law regimes scales approximately as $L_m \propto T^{1/2}$.

2.5 Measurements and Corrections of Nonlinear Optics

2.5.1 First- and Second-Order Chromaticity and Its Correction

Implementation of electron cooling of antiprotons in the Recycler (see Chap. 7) resulted in a dramatic increase of the antiproton beam brightness. After the 2006 shutdown, the head-on beam–beam tune shift experienced by the proton beam exceeded 0.025 and at times reached 0.03 (see Chap. 8). It was then when beam–

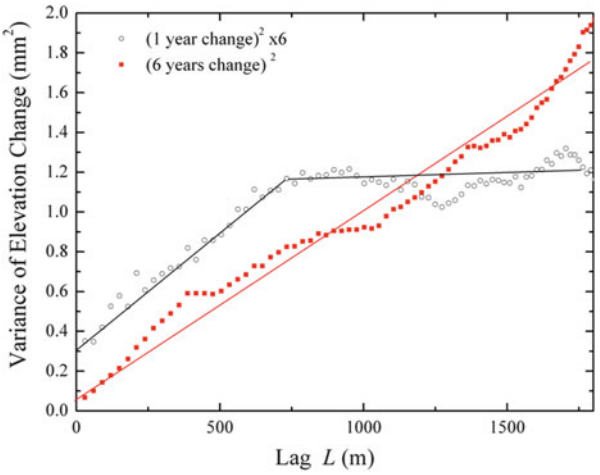

Fig. 2.24 Variances of the Tevatron "tie rod" vertical displacements over time intervals of 1 year (multiplied by 6) and 6 years vs. the distance L [33]

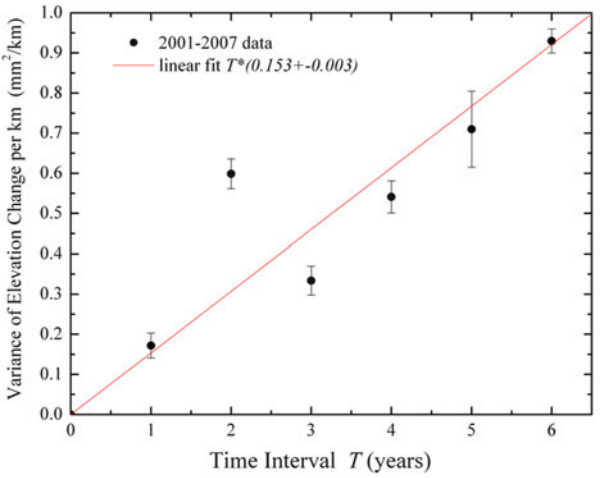

Fig. 2.25 Variances of the Tevatron alignment "tie rods" displacements per unit distance vs. the time interval between the measurements [33]

beam-related losses and emittance blowup started to be observed in protons. It was shown by beam–beam simulations (see Sect. 8.4) that deterioration of the proton lifetime was caused by a decrease of the dynamical aperture for off-momentum particles due to head-on collisions. A contributing factor to this was large chromaticities of the beta-functions at the main IPs.

Initially, a major change of the betatron tune working point was considered as a way to mitigate the beam–beam effect. A possible candidate was the working point near the half-integer resonance, which promised up to 30 % increase of the beam brightness. However, operation near the 1/2 resonance requires careful correction of focusing errors, including the chromatic perturbations. Consequently, it would require machine reproducibility well above achieved and therefore this project was not approved. That motivated the development of a modified chromaticity

correction scheme at the Tevatron, aiming at the reduction of the second-order chromaticity by about an order of magnitude.

One can use the well-known perturbation theory approach to describe the distortion of the beta-function caused by chromatic errors (see e.g., [34]). Beta-beating excited by a single quadrupole for an off-momentum particle can be described by the formula:

$$\frac{\Delta\beta}{\beta}(s) = -\frac{\delta}{2\sin(2\pi Q)}\frac{K}{B\rho}\widetilde{\beta}\cos\left(2|\widetilde{\psi} - \psi(s)| - 2\pi Q\right). \tag{2.134}$$

Here $\delta = \Delta p/p$ is the relative momentum deviation, Q is the betatron tune, K is the quadrupole-integrated strength, $B\rho$ is the magnetic rigidity, ψ is the betatron phase, and ~ denotes values at the location of the quadrupole. In the first-order approximation, the contributions from all quadrupoles are summed to give the total beta-wave. Quadrupoles of the final focus have the largest strength and highest value of beta-function. In the Tevatron, the betatron phase advance between the two interaction regions is close to π; thus, the contributions from the final focus quadrupoles add with the same phase and they dominate the chromatic $\Delta\beta/\beta$.

The contribution to second-order tune chromaticity from a single quadrupole derived from the perturbation theory is given by the following expression:

$$\frac{d^2Q}{d\delta^2} = \left(\frac{1}{4\pi}K\widetilde{\beta}\right)\left(\frac{\Delta\beta}{\beta}/\delta\right). \tag{2.135}$$

This effectively means that the second-order chromaticity is proportional to the strength of the final focus quadrupole and to the value of chromatic beta-function at its location. Figure 2.26 shows the comparison of the measured and modeled chromatic beta-function of the Tevatron in the collision mode. The measured parameters were obtained from two orbit response measurements performed at different values of the revolution frequency. The modeled curve was obtained by the perturbation theory. In Fig. 2.27 the same beta-functions are plotted on a zoomed horizontal scale close to the CDF interaction region. One can see that the model gives quite accurate description of the effect.

Sextupole magnets can be used to correct the second-order chromaticity generated by quadrupole focusing errors. Using the same perturbative approach and considering sextupole as a quadrupole at the off-center orbit, we get the expression for the sextupole-driven horizontal chromatic beta-function:

$$\frac{\Delta\beta}{\beta}(s) = \frac{\delta}{2\sin(2\pi Q)}\frac{S\widetilde{D}_x}{B\rho}\widetilde{\beta}\cos\left(2|\widetilde{\psi} - \psi(s)| - 2\pi Q\right) \tag{2.136}$$

where S is the sextupole strength and ~ denotes parameters at the location of the sextupole. Even though the effect of individual sextupoles on the beta-function chromaticity is much less than that of the final focus quadrupoles, one can achieve

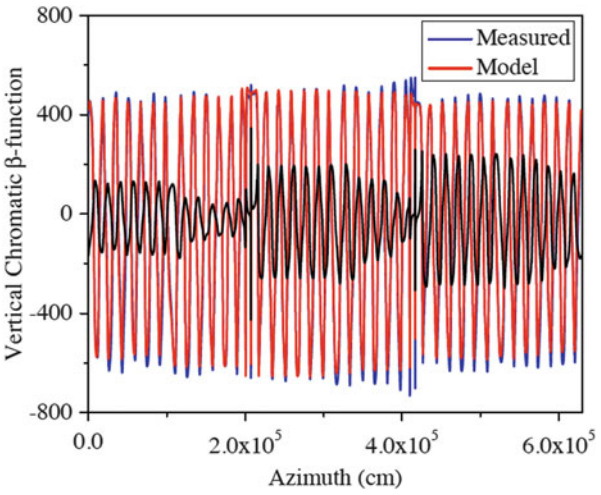

Fig. 2.26 Chromatic beta-function vs. azimuth starting at F0. *Blue line*, measured; *red*, model; *black*, proposed correction

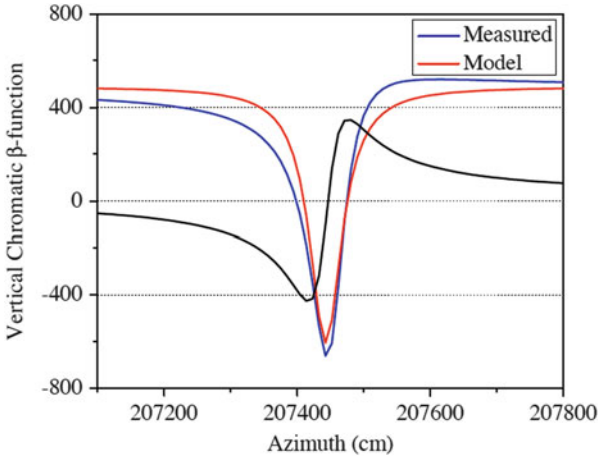

Fig. 2.27 Chromatic beta-function vs. azimuth in the vicinity of CDF IP. *Blue line*, measured; *red*, model; *black*, proposed correction

compensation by selecting many sextupoles with the correct phase advance and combining them into families.

There are 176 chromaticity correction sextupole magnets in the Tevatron. Originally, they were combined into two families SF and SD, each with 88 elements powered in series. Sextupole coils are placed in the so-called spool pieces located next to quadrupoles in the regular FODO lattice of the arcs. The betatron phase advance per FODO cell is close to 60° in both planes. Thus, it was possible to select sextupoles that would have their betatron phase advance with respect to the final focus quads equal to π or $\pi/2$. The total of 46 sextupoles in each family were found to satisfy this condition. However, it was discovered that rewiring them into 4 new circuits would have considerable cost mainly due to the large amount of required new cable. Hence, we had to limit the number of elements in the new circuits and

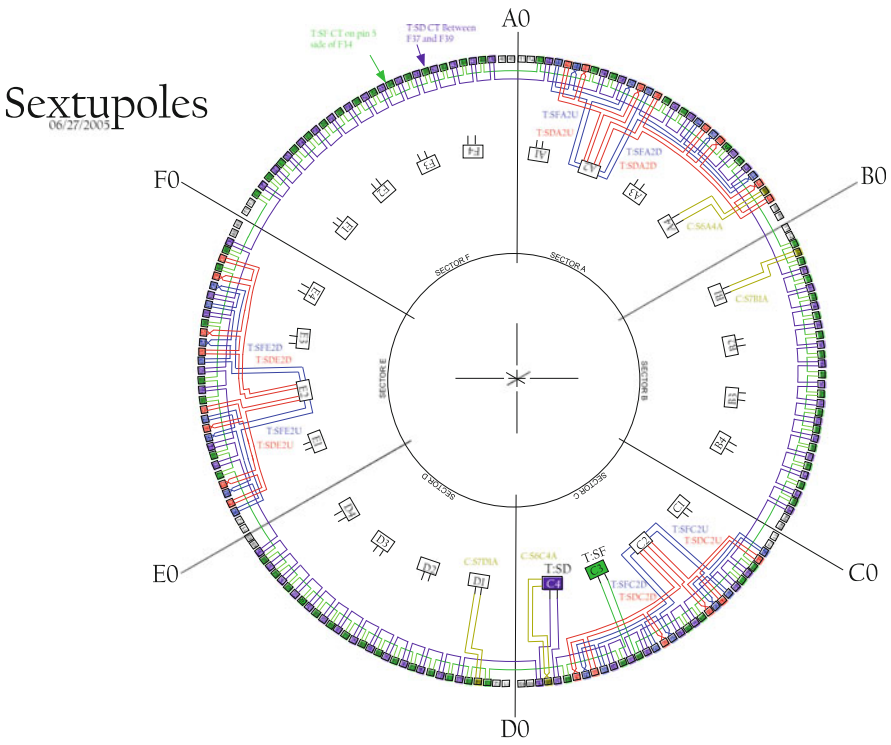

Fig. 2.28 Layout of sextupoles in the Tevatron

group them close to three service buildings which would reduce the length of the new cabling. The final configuration is shown in Fig. 2.28. The total of 44 sextupoles were taken out of the SF and SD families (22 from each). The sextupoles are powered by 12 new power supplies and logically grouped into 4 families. The new circuits are designed to have equal number of elements with positive and negative current. This allows to keep the linear betatron tune chromaticity constant when using the new groups. The disadvantage of this solution is that it breaks the sixfold symmetry of the machine but the expected feed-down effect on the beta-functions is small.

In Figs. 2.26, 2.27, and 2.29, the simulated effect of application of the new families on the chromatic beta-function is plotted for the collision and injection modes. Note that the expected beta-function chromaticity at the CDF IP at collisions is close to zero.

The new sextupole scheme was commissioned in three stages. First, the chosen elements were switched to the new power supplies while being operated at the original current and polarity. This allowed to verify the stability and reliability of electrical components. Second, the new circuits were turned off and the Tevatron was tuned for operating in this new mode. Finally, polarities of some of the

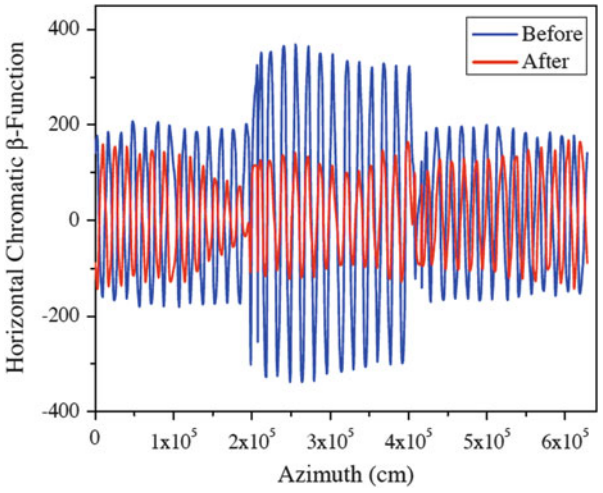

Fig. 2.29 Horizontal chromatic beta-function at the injection energy. *Blue line* is for the original sextupole configuration, *red* for the proposed correction

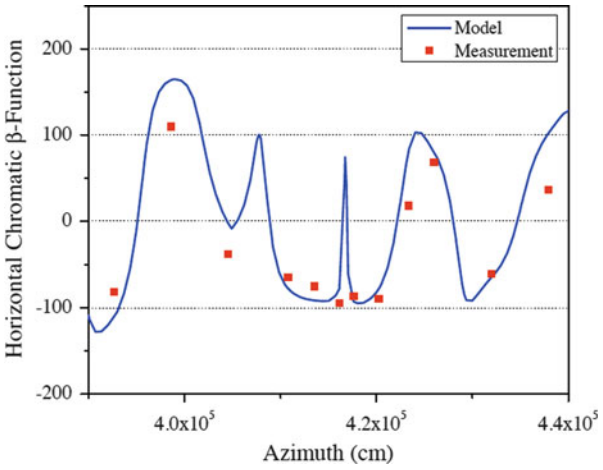

Fig. 2.30 Chromatic beta-function near the D0 IP at the injection energy

sextupoles were flipped and the new families were turned on at the designed strength.

Figures 2.30 and 2.31 show the comparison of expected and measured beta-function chromaticity after implementation of the new circuits in the injection and collision modes, respectively. The corresponding change in the second-order tune chromaticity is presented in Fig. 2.32. Beta-function chromaticities for both the vertical and horizontal planes were corrected.

Measured beta-functions are in good agreement with the calculated values. The second-order tune chromaticity in the collision mode was reduced from $-15{,}000$ units to $-3{,}000$ units which is close to expected. As a result, we observe a noticeable improvement of the proton beam lifetime at collisions (see Chap. 8).

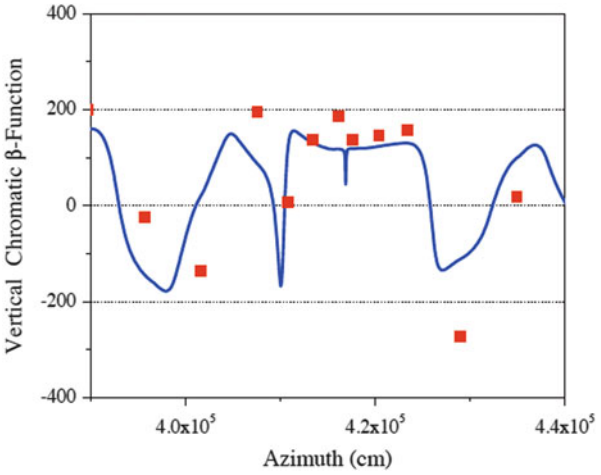

Fig. 2.31 Chromatic beta-function near the D0 IP in the collider mode

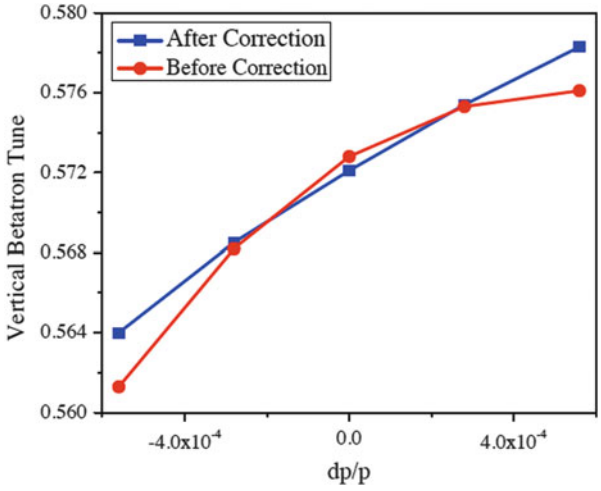

Fig. 2.32 Dependence of the vertical betatron tune on particle momentum in the collider mode

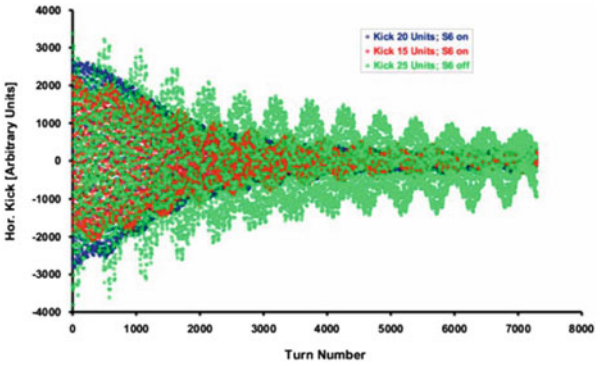

Fig. 2.33 TBT raw data for 7,300 turns after the kick. Three cases are shown: with the sextupoles S6 switched on with $A = 20$ and 15 units and without these special sextupoles for $A = 25$ units

References

1. I. Borchardt, E. Karantzoulis, H. Mais, G. Ripken, Calculation of Beam Envelopes in Storage Rings and Transport Systems in the Presence of Transverse Space Charge Effects and Coupling, DESY 87-161 (DESY, Hamburg, 1987)
2. F. Willeke, G. Ripken, Methods of Beam Optics, in *Proceedings of US Particle Accelerator School (1987 and 1988), AIP Conf. Proc*., New York, 1989, p. 184
3. V. Lebedev, S. Bogacz, JINST **5**, P10010 (2010)
4. L.D. Landau, E.M. Lifshitz, Mechanics (Course of Theoretical Physics, vol. 1) (1976)
5. A.A. Kolomensky, A.N. Lebedev, *Theory of Circular Accelerators* (Moscow, 1962)
6. D.A. Edwards, L.C. Teng, IEEE Trans. Nucl. Sci. **20**(3), 885–889 (1973); L.C. Teng, Fermilab, FN-229 0100 (1971)
7. A. Burov, V. Lebedev, Coupling and Its Effects on Beam Dynamics, in *Proceedings of Hadron Beam 2008*, Nashville, TN
8. A. Burov, Two-beam instability in electron cooling. Phys. Rev. ST-AB **9**, 120101 (2006)
9. V. Lebedev et al., Nucl. Instrum. Meth. **A558**, 299–302 (2006)
10. V. Lebedev, http://www-bdnew.fnal.gov/pbar/organizationalchart/lebedev/OptiM/optim.htm
11. V. Nagaslaev et al., 8 GeV beam line optics optimization for the rapid antiproton transfers at Fermilab, APAC-07, p. 345 (2007)
12. W.J. Corbett, M. Lee, V. Ziemann, in *Proceedings of PAC'93* (Washington, DC, 1993), p. 108
13. J. Safranek, Nucl. Instrum. Meth. **A388**, 27 (1997)
14. ICFA Beam Dynamics Newsletter No. 44 (2007)
15. V. Sajaev, L. Emery, in *Proceeding of EPAC'02* (Paris, France, 2002), p. 742
16. M. Borland, in *Proceedings of ICAP'98* (Monterey, CA, 1998)
17. Y. Alexahin, E. Gianfelice-Wendt, FERMILAB-PUB-06-093-AD (2006)
18. A. Chao et al., Phys. Rev. Lett. **61**, 2752 (1988)
19. T. Satogata et al., Phys. Rev. Lett. **68**, 1838 (1992)
20. T. Chen et al., Phys. Rev. Lett. **68**, 33 (1992)
21. V. Shiltsev et al., Phys. Rev. ST Accel. Beams **8**, 101001 (2005)
22. V. Lebedev et al., Part. Accel. **44**, 147–164 (1994)
23. B.A. Baklakov et al., Tech. Phys. **38**(10), 894–898 (1993); translated from Sov. Zh. Tech. Fiz., **63**(10), 123–132 (1993)
24. V. Shiltsev, Phys. Rev. ST Accel. Beams **13**, 094801 (2010)
25. V. Parkhomchuk, V. Shiltsev, G. Stupakov, Part. Accel. **46**, 241–258 (1994)
26. J. Steimel et al., in *Proceedings of the 2003 I.E. Particle Accelerator Conference* (Portland, OR, 2003), p. 48
27. C.Y. Tan, in *Proceedings of the 2005 I.E. Particle Accelerator Conference* (Knoxville, TN, 2005), p. 141
28. A. Semenov et al., in *Proceedings of IEEE Particle Accelerator Conference* (Albuquerque, NM, 2007), p. 3877
29. V. Shiltsev, G. Stancari, A. Valishev et al., JINST **6**, P08002 (2011)
30. V. Shiltsev, T. Johnson, X.L. Zhang, Preprint FERMILAB-CONF-02-250 (2002)
31. B. Baklakov et al., Phys. Rev. ST-AB **1**, 031001 (1998)
32. C. Moore, in *Proceedings of the IWAA95, KEK-Proc-95/12* (1996), p. 119
33. V. Shiltsev, Phys. Rev. Lett. **104**, 238501 (2010). doi:10.1103/PhysRevLett.104.238501
34. A.W. Chao, M. Tigner, *Handbook of Accelerator Physics and Engineering* (World Scientific, Singapore, 1999), pp. 263–264